

Bayesian estimation of clustered dependence structures in functional neuroconnectivity

Hyoshin Kim¹, Sujit K. Ghosh¹, Adriana Di Martino², and Emily C. Hector ^{*1}

¹Department of Statistics, North Carolina State University

²Autism Center, Child Mind Institute

Abstract

Motivated by the need to model the dependence between regions of interest in functional neuroconnectivity for efficient inference, we propose a new sampling-based Bayesian clustering approach for covariance structures of high-dimensional Gaussian outcomes. The key technique is based on a Dirichlet process that clusters covariance sub-matrices into independent groups of outcomes, thereby naturally inducing sparsity in the whole brain connectivity matrix. A new split-merge algorithm is employed to achieve convergence of the Markov chain that is shown empirically to recover both uniform and Dirichlet partitions with high accuracy. We investigate the empirical performance of the proposed method through extensive simulations. Finally, the proposed approach is used to group regions of interest into functionally independent groups in the Autism Brain Imaging Data Exchange participants with autism spectrum disorder and and co-occurring attention-deficit/hyperactivity disorder.

Keywords: Partition learning, Permutation matrix, Slice sampling, Sparse matrix.

1 Introduction

Analyzing functional connectivity in the brain is a crucial task in the study of Autism Spectrum Disorder (ASD). The specific patterns of hyper- and hypoconnectivity between brain regions of interest (ROIs) of autistic versus neurotypical individuals remains poorly understood, with inconsistent findings regarding abnormal functional connectivity in ASD reported in existing neuroimaging studies [20]. We consider the average resting-state fMRI (rfMRI) time series across voxels in each of M ROIs for individuals $i \in \{1, \dots, n\}$. The individual-specific functional connectivity between M ROIs is estimated by computing the sample correlation between the M averaged rfMRI time series, treating the time series points as independent replicates. In whole-brain analyses, this connectivity matrix is used to investigate patterns of coactivation of ROIs across disease status.

The computational complexity and Type-I error multiplicity associated with the connectivity matrix, which contains $O(M^2)$ entries for each individual, often leads studies to use coarse parcellations with larger ROIs,

^{*}Hector was supported by a grant from the National Science Foundation (DMS2152887) and a Faculty Research and Professional Development Award from North Carolina State University.

such as the Harvard-Oxford atlas with $M = 111$ or the Craddock 200 atlas with $M = 200$ [18, 16]. Studies aiming to investigate brain functional connectivity at a finer scale typically focus on specific sets of brain regions [2, 29], thereby limiting the scope of analyses and scientific discoveries. Moreover, multiple analyses focusing on different sets of brain regions run the risk of type-I error inflation, but multiple comparison adjustments are overly conservative when ROIs are correlated. While whole-brain voxel- or surface-wise analyses are increasingly used, they are computationally expensive and require large scale datasets. There is thus a need for statistical methodology that learns general sparsity patterns in the connectivity matrix of fine brain parcellations and provides appropriate quantification of uncertainty.

Motivated by this need, we aim to identify independent groups of correlated ROIs. Due to the large number of voxels in each ROI, the M averaged rfMRI time series are approximately Gaussian owing to the Central Limit Theorem approximation. Our underlying assumption is that the M outcomes naturally belong to independent groups, leading to a clustering of the covariance sub-matrices. In particular, we assume that the true covariance matrix is a permutation of a block-diagonal matrix composed of structured covariance sub-matrices. This construction ensures that the covariance matrix is positive-definite, capable of accommodating any arbitrary ordering of the ROIs, and flexible in capturing general sparsity patterns. We propose a sampling based Bayesian clustering approach that partitions the covariance matrix of a high-dimensional Gaussian outcome into structured sub-matrices. The independent groups of ROIs identified by our approach can be examined separately in downstream analyses without the fear of loss of statistical power. In Section 5, our method identifies groups of correlated ROIs in individuals diagnosed with Autism Spectrum Disorder (ASD) and attention-deficit/hyperactivity disorder (ADHD) using rfMRI data from the Autism Brain Imaging Data Exchange (ABIDE) [11] preprocessed repository [8]. In this dataset, we use $M = 1000$ ROIs based on the hierarchical multi-resolution parcellation of [42], defining a high-dimensional setting where the number of independent observations, denoted by N , can be comparable to the number of ROIs.

The modeling of high-dimensional covariance matrices has received considerable attention in the literature. Existing methods that assume a group structure for the outcomes typically assume the group structure is predetermined or *a priori* known [26, 28]. Examples in spatial settings include spectral methods [14], tapered covariance functions [23, 44] and low-rank approximations [1, 36]. In contrast, our objective is to learn the group structure through clustering with distinct sets of covariance parameters for each group. Another line of research focused on modeling high-dimensional covariance matrices assumes a general sparsity pattern for the covariance or its inverse, the precision matrix. Bayesian methods in this field use prior distributions that assign zero probability mass to zero entries while concentrating mass on non-zero entries. Examples include the G-Wishart prior [40, 33], the Laplace prior [24, 47], and the spike-and-slab prior [41, 10]. While these methods effectively handle general sparsity patterns, they are more suitable for identifying pairwise relationships between outcomes rather than discovering independent groups of correlated outcomes.

We propose a new Dirichlet process prior for clustering of covariance parameters [13]. To enhance the mixing of cluster components within a Markov chain based sampling procedure, we present a new Metropolis-Hastings split-merge algorithm called the *Head-Tail Split Merge (HTSM)* algorithm. In various applications, split-merge samplers are used alongside Gibbs samplers to improve mixing in models using the Dirichlet process, particularly the Dirichlet process mixture model. The state-of-the-art methods in this domain are the Metropolis-Hastings split-merge samplers proposed by [9] and [22]. Other related approaches include the Metropolis-Hastings Smart-Dumb/Dumb-Smart sampler of [49], which combines smart split moves with

dumb merge moves or vice versa. The Particle Gibbs Split-Merge sampler introduced by [5] avoids the need for complex acceptance ratios in Metropolis-Hastings algorithms. Additionally, [7, 50] focus on parallelization and distribution of Markov Chain Monte Carlo (MCMC) methods applicable to split-merge samplers.

Although these existing split-merge samplers are effective, they are primarily designed for clustering in Dirichlet process mixture models. Typically, such models involve a small number of clusters J and allow for a large dimension M , resulting in larger-sized clusters due to the nature of mixture models. In contrast, our focus is on clustering covariance sub-matrices, where both M and J can be large, allowing for a larger number of smaller-sized clusters, including clusters consisting of a single ROI. To address this scenario, we propose the HTSM algorithm, which can handle these settings effectively. The HTSM algorithm incorporates two types of proposals: a head split-merge proposal used in conjunction with the slice sampler introduced by [46], which is aimed at identifying large clusters, and a tail split-merge proposal employed to detect small clusters. In Section 4, we demonstrate empirically that the proposed algorithm can successfully recover both uniform and true Dirichlet partitions when both M and J are very large. We also show how to incorporate temporal or spatial information to construct the covariance sub-matrices.

The paper is organized as follows. In Section 2, we formulate the Bayesian clustering model for covariance sub-matrices using the stick-breaking representation of the Dirichlet process prior. Section 3 focuses on the sampling of the cluster indices and explores the mixing properties associated with this sampling process. Additionally, this section introduces our proposed HTSM split-merge sampler designed to achieve convergence of the proposed MCMC clustering approach. The results of simulations are presented in Section 4, and an analysis of the ABIDE data is presented in Section 5. Section 6 concludes.

2 A model for clustering covariance sub-matrices

2.1 A model for the independent groups of outcomes

Let $y_i(\mathbf{s}_m)$ be the i -th observed averaged rfMRI outcome at the centroid $\mathbf{s}_m \in \mathbb{R}^3$ of the m -th ROI, $m = 1, \dots, M$, for $i = 1, \dots, N$ independently. In our ABIDE data analysis (Section 5), N corresponds to the total number of (thinned) rfMRI time series for the set of individuals with ASD and ADHD. We define \mathcal{S} as the set of M locations, $\mathcal{S} = \{\mathbf{s}_m\}_{m=1}^M$, and define $\mathbf{y}_i(\mathcal{S}) = \{y_i(\mathbf{s}_1), \dots, y_i(\mathbf{s}_M)\}$, where the order of the ROIs is arbitrary. Let $\{\mathbf{X}_i\}_{i=1}^N$ be N p -dimensional vectors of covariates. We assume that $\mathbb{E}\{\mathbf{y}_i(\mathcal{S})\} = \mathbf{B}\mathbf{X}_i$ with $\mathbf{B} = (\beta_1, \dots, \beta_p) \in \mathbb{R}^{M \times p}$ a matrix of regression parameters, $\beta_q \in \mathbb{R}^M$, $q = 1, \dots, p$. The variance $\mathbb{V}\{\mathbf{y}_i(\mathcal{S})\} = \Sigma(\mathcal{S}, \mathcal{S}; \boldsymbol{\theta})$ depends on a vector of covariance parameters $\boldsymbol{\theta}$ specified below, and does not depend on covariates \mathbf{X}_i . We assume that the outcomes independently follow M -variate Gaussian distributions given by

$$\mathbf{y}_i(\mathcal{S}) \sim \mathcal{N}_M\{\mathbf{B}\mathbf{X}_i, \Sigma(\mathcal{S}, \mathcal{S}; \boldsymbol{\theta})\}.$$

We assume that the outcomes in vector $\mathbf{y}_i(\mathcal{S})$ can be permuted to construct $\mathbf{y}_{i,\text{perm}}(\mathcal{S}) = \{\mathbf{y}_{i,\text{perm}}(\mathcal{S}_1), \dots, \mathbf{y}_{i,\text{perm}}(\mathcal{S}_J)\}$ based on a partition of \mathcal{S} into J sets $\{\mathcal{S}_1, \dots, \mathcal{S}_J\}$, where outcomes $\mathbf{y}_{i,\text{perm}}(\mathcal{S}_j)$ within a group j are correlated with each other and outcomes $\mathbf{y}_{i,\text{perm}}(\mathcal{S}_j), \mathbf{y}_{i,\text{perm}}(\mathcal{S}_{j'})$ across groups j, j' are independent. The independent groups of outcomes induce a block-diagonal structure on $\mathbb{V}\{\mathbf{y}_{i,\text{perm}}(\mathcal{S})\} = \Sigma_{\text{perm}}(\mathcal{S}, \mathcal{S}; \boldsymbol{\theta})$

defined by

$$\Sigma_{\text{perm}}(\mathcal{S}, \mathcal{S}; \boldsymbol{\theta}) = \text{Block-diag}\{\Sigma_{\text{perm}}(\mathcal{S}_1, \mathcal{S}_1; \boldsymbol{\theta}_1), \dots, \Sigma_{\text{perm}}(\mathcal{S}_J, \mathcal{S}_J; \boldsymbol{\theta}_J)\}.$$

The dimension of each diagonal block is denoted by $d_j = |\mathcal{S}_j|$, corresponding to the number of ROIs in the j -th partition set. Each diagonal block covariance matrix $\Sigma_{\text{perm}}(\mathcal{S}_j, \mathcal{S}_j; \boldsymbol{\theta}_j)$ is parameterized by a set of variance and correlation parameters $\boldsymbol{\theta}_j = (\sigma_j^2, \rho_j)$, $j = 1, \dots, J$, and we denote $\boldsymbol{\theta} = (\boldsymbol{\theta}_j)_{j=1}^J \in \mathbb{R}^{2J}$. We model each diagonal block covariance with

$$\Sigma_{\text{perm}}(\mathcal{S}_j, \mathcal{S}_j; \boldsymbol{\theta}_j) = \sigma_j^2 \mathbf{\Gamma}(\mathcal{S}_j, \mathcal{S}_j; \rho_j),$$

where $\mathbf{\Gamma}(\mathcal{S}_j, \mathcal{S}_j; \rho_j)$ is a pre-specified, stationary positive-definite correlation function. This modeling approach allows us to incorporate well-known positive-definite correlation functions, such as compound symmetry, generalized AR(1) [34], or Matérn [30] into our modeling framework.

We introduce the cluster index variable $Z_m \in \{1, \dots, J\}$ to denote the cluster to which the outcome $y_i(\mathbf{s}_m)$ belongs. The cluster indices $\mathbf{Z} = (Z_1, \dots, Z_M)$ induce a partition $\{\mathcal{S}_1, \dots, \mathcal{S}_J\}$, where the number of clusters is determined by $J = \max_m Z_m$. We define a permutation $\pi : \{1, \dots, M\} \rightarrow \{1, \dots, M\}$ which rearranges the elements of \mathbf{Z} in ascending order. The permutation matrix \mathbf{P}_π is constructed by permuting the columns of the identity matrix: the m -th row of \mathbf{P}_π is a standard basis row vector $\mathbf{e}_{\pi(m)} \in \mathbb{R}^M$ with zeros in all entries except for a single 1 located in the $\pi(m)$ -th column. We thus define matrices $\boldsymbol{\pi}$ and \mathbf{P}_π as

$$\boldsymbol{\pi} = \begin{pmatrix} 1 & 2 & \dots & M \\ \pi(1) & \pi(2) & \dots & \pi(M) \end{pmatrix}; \quad \mathbf{P}_\pi = \begin{pmatrix} \mathbf{e}_{\pi(1)} \\ \mathbf{e}_{\pi(2)} \\ \vdots \\ \mathbf{e}_{\pi(M)} \end{pmatrix}.$$

The permutation matrix systematically recovers $\Sigma(\mathcal{S}, \mathcal{S}; \boldsymbol{\theta})$ from $\Sigma_{\text{perm}}(\mathcal{S}, \mathcal{S}; \boldsymbol{\theta})$ through

$$\Sigma(\mathcal{S}, \mathcal{S}; \boldsymbol{\theta}) = \mathbf{P}_\pi^\top \Sigma_{\text{perm}}(\mathcal{S}, \mathcal{S}; \boldsymbol{\theta}) \mathbf{P}_\pi,$$

up to a permutation between blocks, allowing for arbitrary ordering of the diagonal blocks of Σ_{perm} . In this fashion, $\Sigma(\mathcal{S}, \mathcal{S}; \boldsymbol{\theta})$ is equivalent to $\Sigma_{\text{perm}}(\mathcal{S}, \mathcal{S}; \boldsymbol{\theta})$ with its rows and columns permuted. We illustrate with a toy example of a covariance matrix with $M = 50$ in Figure 1.

Our formulation offers several advantages. First, positive-definiteness of estimators of $\Sigma(\mathcal{S}, \mathcal{S}; \boldsymbol{\theta})$ is guaranteed without requiring additional steps or compromising computational efficiency. Second, our approach permits arbitrary ordering of the locations \mathbf{s}_m so that no initial estimate of the partition is required. Third, sparsity estimated in the block-diagonal structure of $\Sigma_{\text{perm}}(\mathcal{S}, \mathcal{S}; \boldsymbol{\theta})$ naturally induces sparsity in $\Sigma(\mathcal{S}, \mathcal{S}; \boldsymbol{\theta})$, enabling our approach to flexibly capture different sparsity patterns. Finally, we allow J to be determined by the data and not pre-fixed.

2.2 Priors for the cluster indices and regression and covariance parameters

We place a Dirichlet process prior on the distribution of the cluster parameters. Let $P \sim \text{DP}(\alpha, P_0)$ denote a Dirichlet process prior distribution [13] with a scale parameter $\alpha > 0$ and a prior probability P_0 .

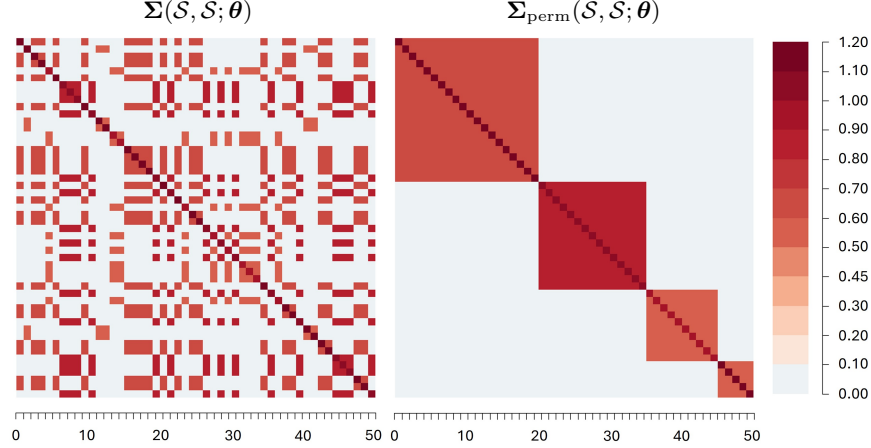


Figure 1: Example $\Sigma(\mathcal{S}, \mathcal{S}; \theta)$ (left) and $\Sigma_{\text{perm}}(\mathcal{S}, \mathcal{S}; \theta)$ (right) for $M = 50$.

We adopt the stick-breaking representation of the Dirichlet process prior [43] as follows:

$$\begin{aligned}
 P &= \sum_{j=1}^{\infty} w_j \delta_{\theta_j}, \quad w_j = V_j \prod_{l=1}^{j-1} (1 - V_l), \\
 \theta_j &\sim P_0 \text{ for } j \in \mathbb{Z}^+, \quad V_j \sim \text{Beta}(1, \alpha) \text{ for } j \in \mathbb{Z}^+,
 \end{aligned} \tag{1}$$

where δ_{\cdot} is a measure with a point mass of 1 at \cdot . This representation makes clear that the distribution P is discrete almost surely. The support of P consists of a countably infinite set of possible values $\{\theta_1, \theta_2, \dots\}$ drawn from the base distribution P_0 , and the weights associated with these values are $\{w_1, w_2, \dots\}$. The term stick-breaking comes from an interpretation of the construction of $\{w_1, w_2, \dots\}$ as consecutively breaking a stick of length 1 into an infinite number of pieces. At the j -th step, the length of the remaining stick is $\prod_{l=1}^{j-1} (1 - V_l)$, and a piece of this stick is broken off according to the random variable $V_j \sim \text{Beta}(1, \alpha)$. The length of the stick we break off at the j -th step is assigned to w_j such that $\sum_{j=1}^{\infty} w_j = 1$ with probability one. The scale parameter α influences the number of clusters produced by the stick-breaking construction, with larger α leading to larger number of clusters on average. We place a conjugate prior on α as $\alpha \sim \text{Gamma}(a_0, b_0)$ as is commonly used for stick-breaking Dirichlet process priors [19, 21, 4].

The prior on the cluster index variable Z_m , $m = 1, \dots, M$, has an explicit form. The index Z_m takes value $j \in \mathbb{Z}^+$ with probability w_j :

$$\Pr(Z_m = j) = w_j \quad \text{for } j \in \mathbb{Z}^+, \quad m = 1, \dots, M.$$

The stick-breaking construction naturally leads to an ordering of the cluster labels based on the sizes of the clusters, due to the fact that $\mathbb{E}(w_j) > \mathbb{E}(w_{j+1})$ for all $j \in \mathbb{Z}^+$ [37]. Throughout this paper, we assume that the cluster labels are arranged in order of decreasing cluster size.

We complete the model formulation by specifying priors for the regression parameters and covariance parameters. We place independent priors on the regression parameters, given by $\beta_q \sim \mathcal{N}_M(0, \tau^2 \mathbf{I}_M)$, $q = 1, \dots, p$, where τ is a hyperparameter to be specified and $\mathbf{I}_M \in \mathbb{R}^{M \times M}$ is the identity matrix. We do not assume an underlying group structure for the regression coefficients β_q . This modeling choice is due to

the nature of our motivating ABIDE data in Section 5, where the covariates are measured at baseline for each individual and do not vary over M . We specify the prior $\sigma_j^2 \sim \text{Inv-Gamma}(a_1, b_1)$ independently for the variance parameters, $j = 1, 2, \dots$. We specify the prior distribution $\eta_j \sim \text{Beta}(a_2, b_2)$ for the correlation parameters, where η_j is a suitable transformation of ρ_j into $(0, 1)$ based on the correlation function $\Gamma(\cdot, \cdot; \rho_j)$, with examples given in Section 4.

2.3 The complete hierarchical model formulation

To avoid the challenging sampling of the infinite-dimensional $\{V_1, V_2, \dots\}$ in equation (1), we propose to use the truncated Dirichlet process introduced by [21]. In this approach, we set V_K to 1, where K is an *a priori* fixed value corresponding to the maximum number of clusters allowed in a partition of \mathcal{S} . By doing so, we ensure that for a sufficiently large K , the infinite sum of stick-lengths, $\sum_{j=1}^{\infty} w_j = 1$, can be transformed into a finite sum, such that $\sum_{j=1}^K w_j = 1$ almost surely. This truncation allows the truncated Dirichlet process to closely approximate the Dirichlet process. We denote the vector of finite-dimensional stick end-points as $\mathbf{V} = (V_1, \dots, V_K)$. By default, we set $K = M$. In situations where M is sufficiently large or when prior knowledge from subject matter science suggests a smaller number of clusters, K can be reduced, e.g. $K = M/2$. Conversely, when M is small, we set K to be large, e.g. $K = 2M$, to minimize the error introduced by the truncation.

The truncation \mathbf{V} leads to the truncation of the number of covariance parameters at K . We therefore define $\boldsymbol{\sigma}^2 = (\sigma_1^2, \dots, \sigma_J^2, \sigma_{J+1}^2, \dots, \sigma_K^2)$ and $\boldsymbol{\rho} = (\rho_1, \dots, \rho_J, \rho_{J+1}, \dots, \rho_K)$. The complete hierarchical model formulation is given by:

$$\begin{aligned}
\alpha &\sim \text{Gamma}(a_0, b_0) \\
\boldsymbol{\beta}_q &\sim \mathcal{N}_M(0, \tau^2 \mathbf{I}_M) \text{ for } q = 1, \dots, p \\
\boldsymbol{\theta}_j &= (\sigma_j^2, \eta_j) \sim \text{Inv-Gamma}(a_1, b_1) \cdot \text{Beta}(a_2, b_2) \text{ for } j = 1, \dots, K \\
V_j | \alpha &\sim \text{Beta}(1, \alpha) \text{ for } j = 1, \dots, K-1 \text{ and } V_K = 1 \\
w_j &= V_j \prod_{l=1}^{j-1} (1 - V_l) \text{ for } j = 1, \dots, K \\
\mathbf{Z} | \mathbf{V} &\sim \text{Categorical}_K\{w(\mathbf{V})\} \\
\boldsymbol{\Sigma}_{\text{perm}}(\mathcal{S}, \mathcal{S}; \boldsymbol{\theta}) &= \text{Block-diag}\{\boldsymbol{\Sigma}_{\text{perm}}(\mathcal{S}_1, \mathcal{S}_1; \boldsymbol{\theta}_1), \dots, \boldsymbol{\Sigma}_{\text{perm}}(\mathcal{S}_J, \mathcal{S}_J; \boldsymbol{\theta}_J)\} \\
\boldsymbol{\Sigma}(\mathcal{S}, \mathcal{S}; \boldsymbol{\theta}) &= \mathbf{P}_{\pi}^{\top} \boldsymbol{\Sigma}_{\text{perm}}(\mathcal{S}, \mathcal{S}; \boldsymbol{\theta}) \mathbf{P}_{\pi} \\
\mathbf{y}_i(\mathcal{S}) | \mathbf{B}, \mathbf{Z}, \boldsymbol{\theta} &\sim \mathcal{N}_M\{\mathbf{B}\mathbf{X}_i, \boldsymbol{\Sigma}(\mathcal{S}, \mathcal{S}; \boldsymbol{\theta})\} \text{ for } i = 1, \dots, N.
\end{aligned}$$

The Gibbs sampler is used to draw samples from the conditional distributions of $\mathbf{V}, \boldsymbol{\sigma}^2, \alpha, \mathbf{B}$, while the slice sampler of [27] is used for the independent sampling of η_j . The step size of the slice sampler is determined by the variance tuning parameter λ , with a larger λ resulting in a larger step size and a smaller λ leading to a smaller step size. We will return to the choice of λ in Section 3 below, where we describe the steps involved in drawing samples of \mathbf{Z} . A comprehensive explanation of the process of sampling from the conditional distributions of $\mathbf{V}, \boldsymbol{\rho}, \boldsymbol{\sigma}^2, \alpha$, and \mathbf{B} using a slice-within-Gibbs sampler is given in Section 1 of the Supplementary Material.

3 Split-merge sampler for cluster indices \mathbf{Z}

3.1 Poor mixing of Gibbs and slice samplers for \mathbf{Z}

Let $\mathbf{Y}(\mathcal{S}) = \{\mathbf{y}_1(\mathcal{S}), \dots, \mathbf{y}_N(\mathcal{S})\} \in \mathbb{R}^{M \times N}$ be the matrix of outcomes, and \mathbf{Z}_{-m} represent the sub-vector of \mathbf{Z} obtained by removing the m -th coordinate. We first consider a Gibbs sampler that draws each Z_m , $m \in \{1, \dots, M\}$, from its conditional posterior distribution, given by

$$p(Z_m = j \mid \mathbf{Z}_{-m}, \cdot) \propto p\{\mathbf{Y}(\mathcal{S}) \mid \mathbf{B}, (Z_1, \dots, Z_{m-1}, j, Z_{m+1}, \dots, Z_M), \boldsymbol{\theta}\} \\ \cdot p\{(Z_1, \dots, Z_{m-1}, j, Z_{m+1}, \dots, Z_M) \mid \mathbf{V}\}, \quad j = 1, \dots, K.$$

Sampling the cluster indices \mathbf{Z} in this fashion results in $O(MK)$ operations at each MCMC iteration, which is computationally intractable when M and/or K is large. The difficulty is exacerbated when the number of clusters J is large, such that a large number of covariance parameters need to be estimated. Further, a large number of MCMC iterations are required to explore the space of partitions of \mathcal{S} due to its size, which corresponds to the Bell [3] number. Indeed, even small values of M , such as $M = 10$, result in a Bell number that exceeds 10^5 . The difficulty in exploring this space efficiently causes many MCMC samplers for models that use the Dirichlet process prior to suffer from poor mixing issues even when the values of M and/or J are relatively small [19].

Walker’s slice sampler [46] offers an alternative solution for drawing samples of Z_m . The sampling steps for Z_m in Walker’s slice sampler are presented in Algorithm 1. At each MCMC iteration, Walker’s slice sampler searches over the cluster indices $\{1, \dots, \min(Z_m + s - 1, K)\}$ for each outcome given some step size $s \in \mathbb{Z}^+$, which requires fewer operations on average compared to the $O(MK)$ complexity of the Gibbs sampler. By default, we set $s = K/2$.

Algorithm 1 Walker’s slice sampler [46] for Z_m

Input: Current values of \mathbf{Z} and $z_0 := Z_m$; support of $Z_m \in \{1, \dots, K\}$; step size $s \in \mathbb{R}^+$

Output: Proposed value of $Z_m := z_1$

1: Define $p_{0|\mathbf{Z}_{-m}, \cdot} = p(Z_m = z_0 \mid \mathbf{Z}_{-m}, \cdot)$. Sample the slice variable $\omega \sim U(0, p_{0|\mathbf{Z}_{-m}, \cdot})$, and sample

$$\ell_1 \sim U\{z_0, \min(z_0 + s - 1, K)\}.$$

2: Set $a = 1$ and $b = \ell_1$.

3: Sample $Z^* \sim U\{a, b\}$. If $p(Z_m = z^* \mid \mathbf{Z}_{-m}, \cdot) > \omega$, accept $z_1 = z^*$. Else,

$$\text{if } z^* < z_0 \text{ then } a = \max(a, z^*) \text{ else } b = \min(b, z^*).$$

4: Repeat Step 3 until $p(Z_m = z^* \mid \mathbf{Z}_{-m}, \cdot) > \omega$ and set $z_1 = z^*$.

Figure 2 illustrates the poor mixing behavior of the commonly used Gibbs sampler and Walker’s slice sampler with an example. It depicts the maximum a posteriori (MAP) estimates of the conditional posterior distribution of \mathbf{Z} obtained using the Gibbs sampler and Walker’s slice sampler. The true partition is generated either from a $\text{DP}(4, P_0)$ distribution ($J = 14$) or from a uniform distribution with equal partition sizes ($J = 20$). The data dimensions are $M = 100$ and $N = 100$, with a generalized AR(1) covariance structure in each cluster – the specific correlation function and covariance parameters are given in Section 4 below. Both

the Gibbs sampler and Walker’s slice sampler have difficulty escaping the local mode of the partition space, resulting in MAP estimates that fail to accurately identify the true partition.

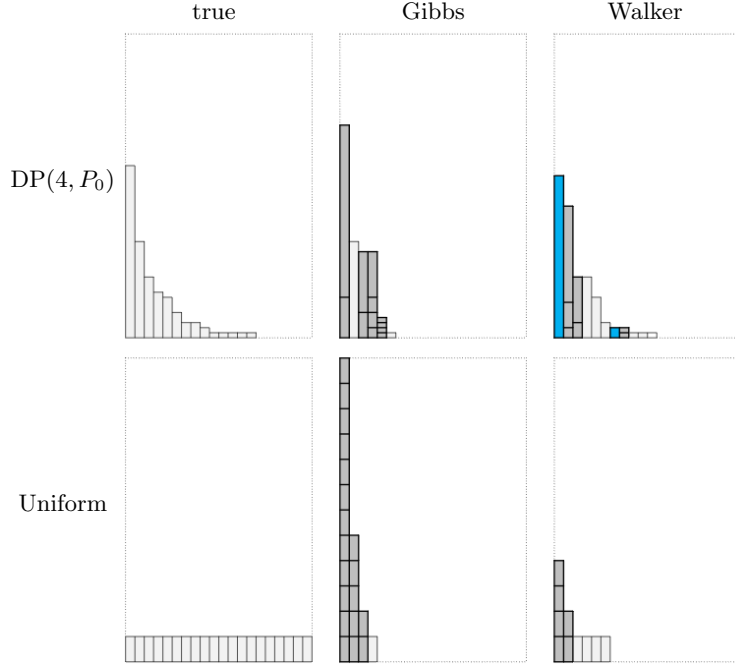


Figure 2: The true partition (left) and MAP estimate of the partition obtained from the Gibbs sampler (middle) and Walker’s slice sampler (right). The true partition is generated from a $DP(4, P_0)$ (top) or a uniform distribution with equal partition sizes (bottom), with $M = 100$ and $N = 100$, assuming a generalized AR(1) covariance structure in each cluster. Highlighted grey bars indicate additional split steps needed to reach the true partition; highlighted blue bars indicate additional merge steps needed to reach the true partition. The MAP estimate of the partition obtained from our proposed clustering method recovers the true partition (see results in Section 4).

In this example, however, Walker’s slice sampler delivers a MAP that is closer to the true partition: it requires fewer split-merge steps to recover the true partition compared to the Gibbs sampler. Split steps involve selecting a cluster and dividing its elements into two clusters, while merge steps involve selecting two clusters and merging them into a single cluster. From Figure 2, we see that i) a larger number of split steps are typically needed to recover the true partition compared to merge steps, and ii) split steps are needed more frequently in clusters of larger and smaller sizes.

These two observations motivate the development of a new sampling algorithm that improves the mixing of Gibbs and Walker’s slice samplers for \mathbf{Z} by performing split-merge steps in addition to Walker’s slice sampler. The Metropolis-Hastings rejection-sampling approach for split-merge steps has been used with standard Gibbs steps to address the issue of slow convergence and poor mixing of the Gibbs sampler [17, 9, 22, 49] for models using the Dirichlet process prior, particularly in the context of Dirichlet process mixture models. Although these existing split-merge samplers have proven effective, they are primarily tailored for settings with a small M and small number of clusters J . In contrast, our focus is on the setting where both M and J are large, potentially with a greater number of small clusters, including single-outcome clusters. To address this high-dimensional setting, we propose the Head-Tail Split-Merge (HTSM) sampler in Section 3.2 below.

3.2 Head-Tail Split-Merge (HTSM) sampler

We define the head of the partition as the larger clusters, and the tail as the smaller clusters. Our proposed HTSM sampler offers two types of split-merge moves: head or tail. A head split-merge is a split or merge move applied to the head of a partition, and a tail split-merge is a split or merge move applied to the tail of a partition. The HTSM sampler is structured into three phases, illustrated in Figure 3. The first and second phases serve as the burn-in period of the MCMC, aimed at reaching convergence of the sampler. The third phase corresponds to the sampling period of the MCMC, where samples are generated for analysis and inference. Specifically:

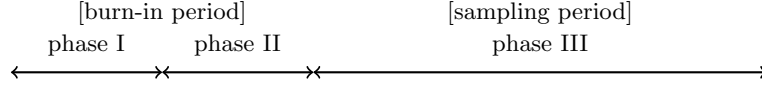


Figure 3: Phases of the proposed HTSM sampler.

- **In phase I of the burn-in period**, we alternate between Walker’s slice sampler and head split-merge moves proposed by our HTSM sampler. The HTSM sampler proposes a head split or merge with probabilities p_0 and $1 - p_0$, respectively. These moves aim to detect larger clusters.
- **In phase II of the burn-in period**, the HTSM sampler proposes tail split-merge moves, where a tail split or merge is proposed with a probability of p_0 or $1 - p_0$, respectively. These moves identify small clusters that may need to be split into smaller clusters.
- **In phase III, the sampling period**, the HTSM sampler proposes tail split-merge moves, where a tail split or merge is proposed with a probability of p_0 or $1 - p_0$, respectively. Further, we increase the variance tuning parameter λ when sampling ρ_j using the slice sampler of Li and Walker [27]. This adjustment is motivated by [19], who observed that samplers become trapped at a partition with high posterior support when insufficient variance is introduced in the sampling. Increasing the variance of the tuning parameter encourages the sampler to explore a broader range of potential partitions by introducing greater variability in ρ_j and, subsequently, in \mathbf{Z} .

In each iteration of the MCMC, in addition to employing the HTSM sampler for \mathbf{Z} , we use the slice-within-Gibbs sampler as outlined in Section 1 of the Supplementary Material to sample the remaining parameters. Following the completion of the HTSM sampler in each iteration, we conduct a relabeling of \mathbf{Z} . This relabeling step is crucial to ensure the cluster labels are sorted from the largest to the smallest cluster.

The proposed HTSM sampler is outlined in Algorithm 2. Our approach uses p_0 to decide between a split or merge move, allowing us to control the proportion of split and merge moves. We set the default value of p_0 to 0.7 to encourage split moves to occur more frequently than merge moves. Our approach of using p_0 differs from [22] and [9], where a pair of indices are uniformly chosen to determine a split or merge move based on whether the selected pair is in the same cluster or not. [49] used a similar approach to ours by pre-selecting the split-merge move type, but they chose their split-merge moves uniformly. As we show in Section 4, these differences have substantial benefits for the convergence of our sampler.

On the one hand, the split step across the three phases is characterized by two different vectors that encourage splitting in the large versus small clusters, respectively. On the other hand, merge steps across both phases give equal probability to all clusters, regardless of their size, to be merged. Below, we describe

the probability vectors that favor large and small clusters, as well as the implementation details for the split-merge moves. Let \mathbf{Z}^* and $\boldsymbol{\theta}^*$ be the candidate states which we will consider for the split-merge proposal. Denote J^+ as the number of clusters of size greater than one.

Algorithm 2 Head-Tail Split-Merge sampler

Input: Current values of $\mathbf{Z}, \boldsymbol{\theta}$; split-merge probability p_0 ; $\text{type}_{HT} \in \{\text{Head}, \text{Tail}\}$

Output: Proposed values of $\mathbf{Z}, \boldsymbol{\theta}$

- 1: Set candidate states as \mathbf{Z}^* and $\boldsymbol{\theta}^*$.
- 2: Choose the split-merge move type with probability

$$\Pr(\text{Split}) = p_0 \text{ and } \Pr(\text{Merge}) = 1 - p_0.$$

- 3: If Split:

If $\text{type}_{HT} = \text{Head}$, then $\mathbf{p}_{\text{split}} \in \mathbb{R}^{J^+}$ is a decreasing probability vector.

Else if $\text{type}_{HT} = \text{Tail}$, then $\mathbf{p}_{\text{split}} \in \mathbb{R}^{J^+}$ is an increasing probability vector.

Choose the j -th cluster to split according $\mathbf{p}_{\text{split}}$.

Prepare the launch state by randomly assigning indices $\{Z_m^*\} = \{Z_m^* : Z_m^* = j\}$ into one of the two clusters: j or $(J+1)$.

Set $\theta_{j+1}^* := \theta_j^*$.

Assign $\{Z_m^*\}$ sequentially into the j or $(J+1)$ -th cluster according to probabilities

$$p(Z_m^* = j | \mathbf{Z}_{-m}^*, \boldsymbol{\theta}^*, \cdot) \text{ and } p(Z_m^* = J+1 | \mathbf{Z}_{-m}^*, \boldsymbol{\theta}^*, \cdot).$$

- 4: Else if Merge:

Choose the j and j' -th clusters to merge uniformly from the J clusters.

Assign the indices $\{Z_m^* : Z_m^* = j\}$ and $\{Z_m^* : Z_m^* = j'\}$ to the j -th cluster.

Set $\theta_{j'}^* := \theta_j^*$.

- 5: Calculate the Metropolis-Hastings acceptance probability

$$\alpha^* = \min \left[1, \frac{q\{(\mathbf{Z}, \boldsymbol{\theta}) | (\mathbf{Z}^*, \boldsymbol{\theta}^*), \cdot\} p\{\mathbf{Y}(S) | \mathbf{Z}^*, \boldsymbol{\theta}^*, \cdot\} p(\mathbf{Z}^* | \mathbf{V}) p(\boldsymbol{\theta}^*)}{q\{(\mathbf{Z}^*, \boldsymbol{\theta}^*) | (\mathbf{Z}, \boldsymbol{\theta}), \cdot\} p\{\mathbf{Y}(S) | \mathbf{Z}, \boldsymbol{\theta}, \cdot\} p(\mathbf{Z} | \mathbf{V}) p(\boldsymbol{\theta})} \right],$$

and accept the proposal with probability α^* .

In the event of a head or tail merge proposal, where $(\mathbf{Z}^*, \boldsymbol{\theta}^*) = (\mathbf{Z}^{\text{merge}}, \boldsymbol{\theta}^{\text{merge}})$, the sampler selects two clusters, the j -th and the j' -th cluster uniformly at random from the set of J clusters. The indices $\{Z_m^* : Z_m^* = j\}$ and $\{Z_m^* : Z_m^* = j'\}$ within both clusters are then assigned to the j -th cluster, with the covariance parameter $\boldsymbol{\theta}_{j'}^*$ updated by setting it equal to $\boldsymbol{\theta}_j^*$.

In the case of a head or tail split proposal, where $(\mathbf{Z}^*, \boldsymbol{\theta}^*) = (\mathbf{Z}^{\text{split}}, \boldsymbol{\theta}^{\text{split}})$, the initial step involves constructing a probability vector $\mathbf{p}_{\text{split}} \in \mathbb{R}^{J^+}$. On the one hand, if a head split is proposed, a decreasing probability vector $\mathbf{p}_{\text{split}} \in \mathbb{R}^{J^+}$ is constructed, with a preference for selecting larger clusters for the split move. On the other hand, if a tail split is proposed, an increasing probability vector $\mathbf{p}_{\text{split}} \in \mathbb{R}^{J^+}$ is constructed, and a cluster to split is randomly chosen based on this vector, resulting in a tendency to choose smaller clusters.

After selecting the j -th cluster for splitting according to $\mathbf{p}_{\text{split}}$, we prepare the launch state by randomly assigning the indices $\{Z_m^*\} = \{Z_m^* : Z_m^* = j\}$ within that cluster to either the same j -th cluster or a new $(J+1)$ -th cluster. Additionally, the covariance parameter θ_{j+1}^* is updated by assigning it the value of θ_j^* . Then, the indices $\{Z_m^*\}$ are sequentially assigned to one of the two clusters according to the conditional

posterior distributions $p(Z_m^* = j | \mathbf{Z}_{-m}^*, \boldsymbol{\theta}^*, \cdot)$ and $p(Z_m^* = J + 1 | \mathbf{Z}_{-m}^*, \boldsymbol{\theta}^*, \cdot)$ using the restricted Gibbs sampler.

It remains to calculate the Metropolis-Hastings acceptance probability for the HTSM sampler, which takes the form

$$\alpha^* = \min \left[1, \frac{q\{(\mathbf{Z}, \boldsymbol{\theta}) | (\mathbf{Z}^*, \boldsymbol{\theta}^*), \cdot\} p\{\mathbf{Y}(S) | \mathbf{Z}^*, \boldsymbol{\theta}^*, \cdot\} p(\mathbf{Z}^* | \mathbf{V}) p(\boldsymbol{\theta}^*)}{q\{(\mathbf{Z}^*, \boldsymbol{\theta}^*) | (\mathbf{Z}, \boldsymbol{\theta}), \cdot\} p\{\mathbf{Y}(S) | \mathbf{Z}, \boldsymbol{\theta}, \cdot\} p(\mathbf{Z} | \mathbf{V}) p(\boldsymbol{\theta})} \right], \quad (2)$$

where $(\mathbf{Z}^*, \boldsymbol{\theta}^*)$ is either $(\mathbf{Z}^{\text{split}}, \boldsymbol{\theta}^{\text{split}})$ or $(\mathbf{Z}^{\text{merge}}, \boldsymbol{\theta}^{\text{merge}})$ depending on the type of proposal, and $q\{(\mathbf{Z}, \boldsymbol{\theta}) | (\mathbf{Z}^*, \boldsymbol{\theta}^*), \cdot\}$ and $q\{(\mathbf{Z}^*, \boldsymbol{\theta}^*) | (\mathbf{Z}, \boldsymbol{\theta}), \cdot\}$ are transition probabilities from $(\mathbf{Z}^*, \boldsymbol{\theta}^*)$ to $(\mathbf{Z}, \boldsymbol{\theta})$ and from $(\mathbf{Z}, \boldsymbol{\theta})$ to $(\mathbf{Z}^*, \boldsymbol{\theta}^*)$ respectively. Here, we factored the posterior distribution into a product of the likelihood and the prior, and ignored terms not involving $(\mathbf{Z}, \boldsymbol{\theta})$ or $(\mathbf{Z}^*, \boldsymbol{\theta}^*)$. A graphical presentation of the transition probabilities for HTSM split-merge proposals is shown as a directed acyclic graph (DAG) in Figure 4. We can calculate the individual terms in Equation (2) as follows.

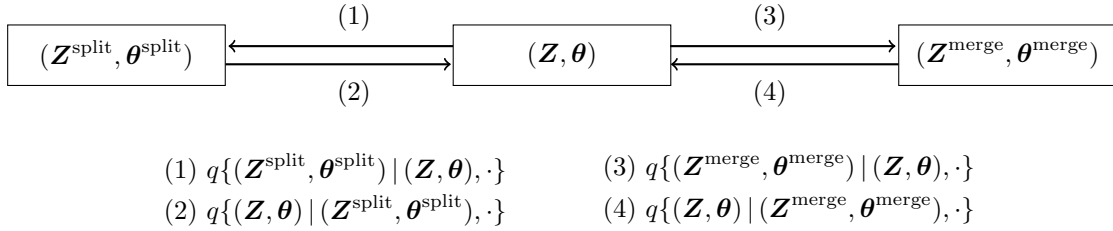


Figure 4: The DAG presenting the transition probabilities for a split-merge proposal of the HTSM.

- The split proposal probability $q\{(\mathbf{Z}^{\text{split}}, \boldsymbol{\theta}^{\text{split}}) | (\mathbf{Z}, \boldsymbol{\theta}), \cdot\}$ can be expressed as

$$\begin{aligned} q\{(\mathbf{Z}^{\text{split}}, \boldsymbol{\theta}^{\text{split}}) | (\mathbf{Z}, \boldsymbol{\theta}), \cdot\} &= q\{\mathbf{Z}^{\text{split}} | \boldsymbol{\theta}^{\text{split}}, (\mathbf{Z}, \boldsymbol{\theta}), \cdot\} q\{\boldsymbol{\theta}^{\text{split}} | (\mathbf{Z}, \boldsymbol{\theta}), \cdot\} \\ &= q(\mathbf{Z}^{\text{split}} | \boldsymbol{\theta}^{\text{split}}, \mathbf{Z}, \cdot) \\ &= \left(\frac{1}{2}\right)^{d_j} \prod_{m \in \mathcal{I}_{d_j}} p(Z_m = z_m^{\text{split}} | \mathbf{Z}_{-m}, \boldsymbol{\theta}^{\text{split}}, \cdot), \end{aligned}$$

where \mathcal{I}_{d_j} denotes the set of coordinates for the launch state, with a size of d_j . The second equality is derived by observing that splitting the cluster indices vector is only influenced by $(\mathbf{Z}, \boldsymbol{\theta}^{\text{split}})$, and not by $\boldsymbol{\theta}$. Additionally, $q\{\boldsymbol{\theta}^{\text{split}} | (\mathbf{Z}, \boldsymbol{\theta}), \cdot\} = 1$ since, given $(\mathbf{Z}, \boldsymbol{\theta})$, there is only one way to obtain $\boldsymbol{\theta}^{\text{split}}$, which is to set $\theta_{J+1}^{\text{split}} := \theta_j^{\text{split}}$. The last equality is the multiplication of two terms: the first term represents the probability of proposing a split move from the original state to the launch state $(1/2^{d_j})$. The second term is the product of the sequential allocation proposal probabilities from the launch state to the split state. Specifically, each $p(Z_m = z_m^{\text{split}} | \mathbf{Z}_{-m}, \boldsymbol{\theta}^{\text{split}}, \cdot)$ denotes the probability that Z_m , the cluster index in the launch state, is allocated to the observed cluster index z_m^{split} in the split state, where z_m^{split} is either j or $J + 1$. The product is calculated sequentially for all $m \in \mathcal{I}_{d_j}$.

- The reverse merge proposal probability is calculated as $q\{(\mathbf{Z}, \boldsymbol{\theta}) | (\mathbf{Z}^{\text{split}}, \boldsymbol{\theta}^{\text{split}}), \cdot\} = 1/J$. This probability is determined by uniformly selecting one cluster from a set of J clusters for merging, while keeping the second cluster fixed as the $(J + 1)$ -th cluster. The two clusters are then merged into the first cluster that

was chosen.

- The merge proposal probability is calculated as $q\{(\mathbf{Z}^{\text{merge}}, \boldsymbol{\theta}^{\text{merge}}) | (\mathbf{Z}, \boldsymbol{\theta}), \cdot\} = 1/\{J(J-1)\}$. The proposal uniformly selects two clusters from a set of J clusters, and merges the two clusters into the first cluster that was chosen.
- The reverse split proposal probability $q\{(\mathbf{Z}, \boldsymbol{\theta}) | (\mathbf{Z}^{\text{merge}}, \boldsymbol{\theta}^{\text{merge}}), \cdot\}$ is calculated in the same way as the split proposal probability as:

$$\begin{aligned} q\{(\mathbf{Z}, \boldsymbol{\theta}) | (\mathbf{Z}^{\text{merge}}, \boldsymbol{\theta}^{\text{merge}}), \cdot\} &= q\{\mathbf{Z} | \boldsymbol{\theta}, (\mathbf{Z}^{\text{merge}}, \boldsymbol{\theta}^{\text{merge}}), \cdot\} q\{\boldsymbol{\theta} | (\mathbf{Z}^{\text{merge}}, \boldsymbol{\theta}^{\text{merge}}), \cdot\} \\ &= q(\mathbf{Z} | \boldsymbol{\theta}, \mathbf{Z}^{\text{merge}}, \cdot) \\ &= \left(\frac{1}{2}\right)^{d_j} \prod_{m \in \mathcal{I}_{d_j}} p(Z_m^{\text{merge}} = z_m | \mathbf{Z}_{-m}^{\text{merge}}, \boldsymbol{\theta}, \cdot) \end{aligned}$$

where \mathcal{I}_{d_j} denotes the set of coordinates for the launch state, with a size of d_j .

3.3 Convergence of hybrid samplers

Li and Walker’s slice sampler [27], employed for sampling the correlation parameters η_j , is an extension of Neal’s well-known slice sampler [35], featuring a modified search component. Additionally, Walker’s slice sampler [46], used for sampling the cluster indices \mathbf{Z} , is an adaptation of Li and Walker’s slice sampler tailored for discrete sample spaces. The convergence properties of slice samplers have been thoroughly investigated. [39] demonstrated the geometric ergodic properties of slice samplers, while [32] established a sufficient condition for the uniform ergodicity of slice samplers. Moreover, [46] showed the convergence of their proposed transition density to the stationary distribution when the step size is large. The ergodicity of the HTSM sampler is ensured as it operates as a Metropolis-Hastings split-merge algorithm [31]. For an in-depth discussion on the ergodicity of Metropolis-Hastings split-merge algorithms, refer to Section 3.4 of Neal [35].

Our sampling approach involves a hybrid sampler, combining Walker’s slice sampler, Li and Walker’s slice sampler, Gibbs sampler, and the HTSM sampler. The convergence of hybrid samplers involving multiple distinct MCMC algorithms has been extensively investigated. As detailed in Section 2.4 of Tierney [45], combining Metropolis-Hastings and Gibbs sampling steps yields an ergodic Markov chain. Following the findings of Mira and Tierney [32], the slice-within-Gibbs sampler also maintains ergodicity.

4 Numerical illustrations using simulated data

Two sets of simulated data scenarios with large values of M and J are explored. To mimic our real data example, we set N to be of the same order as M . In the first simulation, the true partition is generated from a Uniform distribution with equal cluster sizes. In the second simulation, the true partition is generated from a Dirichlet process prior. We consider three correlation functions $\boldsymbol{\Gamma}(\cdot, \cdot; \rho_j)$ at various points throughout the two simulations: Matérn, generalized AR(1) and compound symmetry, described below. In each simulation, results are compared across 50 simulated data sets each run for 10,000 MCMC iterations. The burn-in period, comprising two phases, consists of 1,000 iterations each, resulting in a total of 2,000 iterations. The

remaining 8,000 iterations are allocated for the sampling period. Throughout the burn-in period, the variance tuning parameter λ for ρ_j is set to 100, while during the sampling period, it is set to 150.

In both simulations, \mathbf{X}_i consists of $p = 5$ covariates, including an intercept X_{i1} . The covariates X_{i2} and X_{i3} are generated from Bernoulli distributions with success probabilities of 0.5 and 0.7, respectively. The covariate X_{i4} is generated from a standard Gaussian distribution, and the last covariate X_{i5} is the interaction term between X_{i2} and X_{i4} . We specify the maximum number of allowable clusters K to be $M/2$. The prior specifications include setting $\tau = 1$ for the prior on regression coefficients, $\beta_q \sim \mathcal{N}_M(\mathbf{0}, \mathbf{I}_M)$, $q = 1, \dots, p$. The variance parameters have prior distribution $\sigma_j^2 \sim \text{Inv-Gamma}(2.01, 1.01)$, and the transformed correlation parameters have prior distribution $\eta_j \sim \text{Beta}(2.01, 1.01)$. With the Matérn and generalized AR(1) correlation functions, ρ_j lies in $(0, 1)$, so $\eta_j = \rho_j$. With the compound symmetry correlation function, $\rho_j \in (-1/(d_j - 1), 1)$, and its support depends on \mathbf{Z} . This poses challenges when updating ρ_j during the MCMC since the support changes. To address this, we slightly narrow the support to $\rho_j \in (-1/(M - 1), 1)$, which ensures positive-definiteness of covariance matrices while maintaining a constant support throughout the iterations. The corresponding transformation is $\eta_j = (M - 1)\rho_j/M + 1/M$. It is worth noting that the upper bound for the support of ρ_j is typically 1 for most covariance structures. To avoid computational issues arising from near-singular correlation sub-matrices, we set the upper bound for ρ_j to be 0.95. The Dirichlet process scale parameter is assigned the prior $\alpha \sim \text{Gamma}(K + 0.01, 1.01)$. This choice ensures that the prior mean for α is approximately equal to K , effectively setting the initial number of clusters as large as possible. As discussed in [19], it is recommended to set the initial number of clusters to be large in order to achieve convergence of the posterior distribution of α .

For a head split proposal in the HTSM sampler, we set $\mathbf{p}_{\text{split}}$ such that the approximate probabilities of selecting clusters for splitting are as follows: about 0.3 for the largest cluster, about 0.2 for the second largest cluster, about 0.15 for the third largest cluster, and about 0.1 for the fourth largest cluster. This configuration results in around 75% of the split moves occurring within these four largest clusters. Conversely, for a tail split proposal in the HTSM sampler, we configure $\mathbf{p}_{\text{split}}$ to be the reverse of that in the head split proposal.

In the first simulation, the performance of the model is evaluated when the true partition is from a Uniform distribution with equal cluster sizes, $J = M/5$. We consider three different settings. The first setting considers dimensions $M = 500$ and $N = 500$ with a homogeneous compound symmetric (CS) covariance structure, where the same ρ and σ^2 are assumed for all clusters. The true ρ and σ^2 are set to 0.7 and 1.1, respectively. The second setting also considers dimensions $M = 500$ and $N = 500$, but with a more complex heterogeneous generalized AR(1) covariance structure [34]. Here, different sets of ρ_j and σ_j^2 are assumed for each cluster. For each cluster, the true ρ_j is sampled from a uniform sequence with a spacing of 0.05 between 0.4 and 0.9, and the true σ_j^2 is sampled from a uniform sequence with a spacing of 0.05 between 0.95 and 1.5. The generalized AR(1) covariance structure is defined by:

$$\text{Cov}\{y_i(\mathbf{s}_\ell), y_i(\mathbf{s}_k)\} = \sigma_j^2 \rho_j^{\{d(\mathbf{s}_\ell, \mathbf{s}_k)\}^\nu} \mathbb{1}(\ell \neq k) + \sigma_j^2 \mathbb{1}(\ell = k).$$

Here, $\mathbf{s}_m \equiv s_m \in \mathbb{R}$, $m = 1, \dots, M$ with $d(\mathbf{s}_\ell, \mathbf{s}_k)$ the Euclidean distance between two locations. The decay speed parameter is set to $\nu = 0.2$. The third and most complicated setting considers dimensions $M = 1000$ and $N = 1000$, and uses a heterogeneous Matérn covariance structure [30] with shape parameter $\nu = 1.5$,

given by

$$\text{Cov}\{y_i(\mathbf{s}_\ell), y_i(\mathbf{s}_k)\} = \sigma_j^2 \left\{ 1 + \frac{\sqrt{3}d(\mathbf{s}_\ell, \mathbf{s}_k)}{\rho_j} \right\} \exp\left\{ -\frac{\sqrt{3}d(\mathbf{s}_\ell, \mathbf{s}_k)}{\rho_j} \right\} \mathbb{1}(\ell \neq k) + \sigma_j^2 \mathbb{1}(\ell = k).$$

Each ρ_j and σ_j^2 is generated in the same manner as in the second setting. Here, $\mathbf{s}_m \in \mathbb{R}^2$, with $d(\mathbf{s}_\ell, \mathbf{s}_k)$ the Euclidean distance between two locations divided by 20.

Figure 5 displays the posterior of the number of clusters across the three settings. As the complexity of the covariance structure increases, the convergence of the sampler requires a higher number of iterations. During the burn-in period, the MAP estimate in all 50 simulations of homogeneous CS correctly identified the true partition. For the heterogeneous AR(1) setting, the MAP estimate corresponded to the true partition in 49 out of 50 simulations, while in the heterogeneous Matérn setting, it corresponded to the true partition in 48 out of 50 simulations. During the sampling period, for all three settings, the MAP estimate corresponded to the true partition in all 50 simulations.

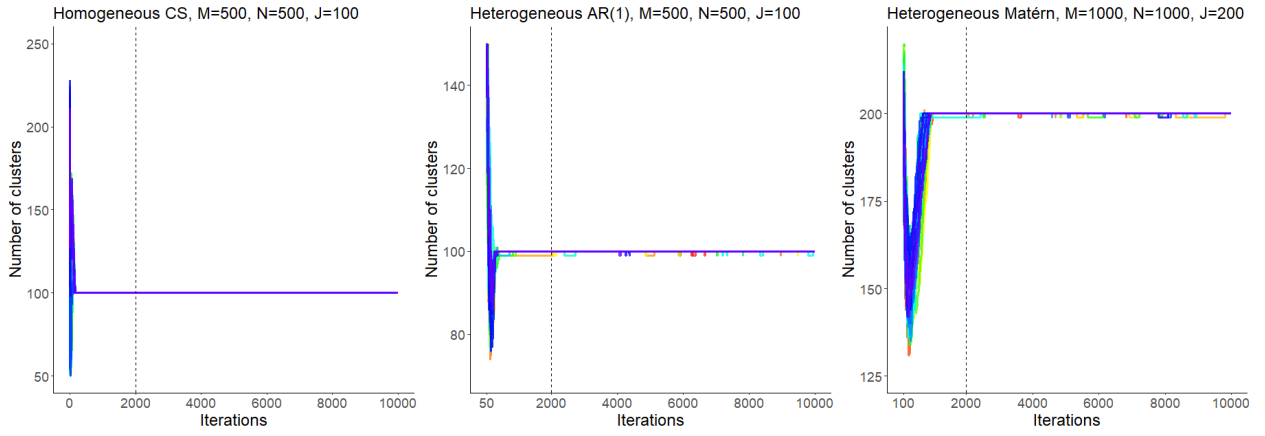


Figure 5: First simulation – Plot of the posterior of the number of clusters for the 50 simulations conducted over 10,000 iterations, assuming a uniform true partition. Each line represents the posterior number of clusters for an individual simulation. The vertical dotted line at iteration 2,000 indicates the end of the burn-in period.

Table 1 presents the average coverage rates for a 95% credible interval across 50 simulations for $\boldsymbol{\rho}$, $\boldsymbol{\sigma}^2$ and \mathbf{B} during the sampling period. The results indicate that the desired 95% level is achieved for all three settings, with slightly conservative inference. In the homogeneous CS setting, the dimensions of $\boldsymbol{\rho}$ and $\boldsymbol{\sigma}^2$ are both one, making it relatively easy for the model to identify the distribution of these two parameters accurately. It should be noted that the coverage rates for $\boldsymbol{\rho}$, $\boldsymbol{\sigma}^2$, \mathbf{B} are computed from the subset of iterations where \mathbf{Z} is equal to its MAP estimate. This is because the posterior distributions for $\boldsymbol{\rho}$, $\boldsymbol{\sigma}^2$, and \mathbf{B} depend on the value of \mathbf{Z} . When the estimate of \mathbf{Z} is close to the true partition, the conditional posterior distributions are likely centered around the true values. Conversely, for estimates of \mathbf{Z} that are farther from the true partition, the posterior distributions are likely centered around other values, leading to multi-modal marginal posterior distributions.

In the second simulation, we consider two settings with the true partition from a $\text{DP}(6, P_0)$. The first setting has dimensions $M = 500$, $N = 500$, $J = 23$, and a heterogeneous CS covariance structure. The second

Table 1: First simulation – Coverage rate (standard deviation) of 95% credible interval for each parameter, averaged across 50 simulations during the sampling period, assuming a uniform true partition. The coverage rates for ρ , σ^2 , \mathbf{B} are computed from the subset of iterations where \mathbf{Z} is equal to its MAP estimate.

	M	N	J	coverage rate (sd)		
				ρ	σ^2	\mathbf{B}
homogeneous CS	500	500	100	1.00 (0.00)	1.00 (0.00)	0.95 (0.01)
heterogeneous AR(1)	500	500	100	0.97 (0.02)	0.96 (0.02)	0.95 (0.01)
heterogeneous Matérn	1000	1000	200	0.98 (0.01)	0.98 (0.01)	0.95 (0.01)

setting also has a heterogeneous CS covariance structure, but with larger dimensions $M = 1000$, $N = 1000$, and $J = 37$. The sets of ρ_j and σ_j^2 are sampled in the same way as in the first simulation. This setting allows for a small number of very large clusters and a moderate number of size one clusters in the true partition.

Figure 6 illustrates the posterior distribution of the number of clusters across the two settings. Throughout the burn-in phase, the MAP estimate consistently identified the true partition in all 50 simulations in both settings. During the subsequent sampling phase, the MAP estimate corresponded to the true partition in all 50 simulations of the heterogeneous CS with $M = 1000$ setting, and in 42 out of 50 simulations of the heterogeneous CS with $M = 500$ setting.

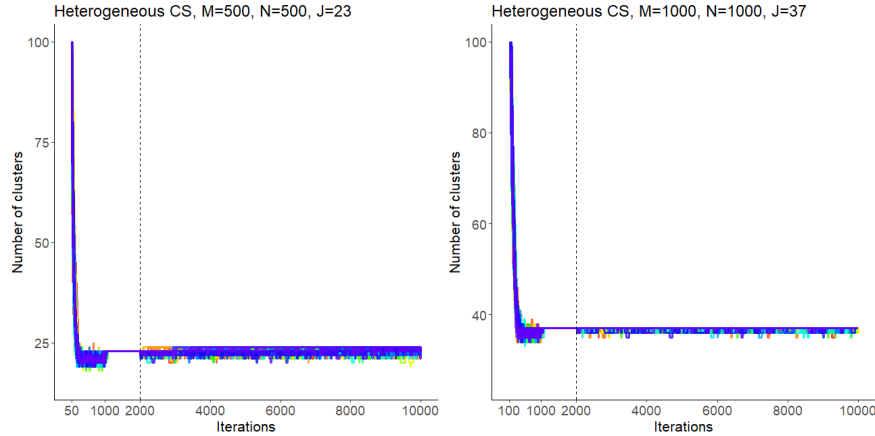


Figure 6: Second simulation – Plot of the posterior of the number of clusters for the 50 simulations conducted over 10,000 iterations, assuming a $\text{DP}(6, P_0)$ true partition. Each line represents the posterior number of clusters for an individual simulation. The vertical dotted line at iteration 2,000 indicates the end of the burn-in period.

Table 2 displays the average coverage rates of 95% credible intervals across 50 simulations for ρ , σ^2 , and \mathbf{B} during the sampling period. The desired 95% level of coverage was achieved for all parameters in both settings.

The increased variability during the sampling phase in both settings of the second simulation can be attributed to setting the variance tuning parameter of the slice sampler for ρ_j to $\lambda = 150$. By increasing λ , the sampler exhibits more variability, allowing it to explore a wider range of potential partitions. However, this increased variability also means that the MAP estimate may not always match the true partition for some simulations. Nevertheless, it is important to note that the 95% credible interval for \mathbf{Z} across all 50 simulations contains the true partition in each setting.

Table 2: Second simulation – Coverage rate (standard deviation) of 95% credible interval for each parameter, averaged across 50 simulations during the sampling period, assuming a $DP(6, P_0)$ true partition. The coverage rates are computed from the subset of iterations where \mathbf{Z} is equal to its MAP estimate.

	M	N	J	coverage rate (sd)		
				ρ	σ^2	B
heterogeneous CS	500	500	23	0.97 (0.04)	0.96 (0.04)	0.95 (0.02)
heterogeneous CS	1000	1000	37	0.98 (0.02)	0.97 (0.03)	0.95 (0.02)

The second simulation only considers the CS covariance structure. When we consider covariance functions that rely on distances between measurements, estimating the true partition becomes challenging, particularly when dealing with large cluster sizes. In the case of a very large cluster, even with a slow decay rate, the off-diagonal terms of the covariance sub-matrix can be small, making it difficult to differentiate this covariance matrix from a combination of several moderately sized sub-matrices. It is important to highlight that this challenge primarily arises in high-dimensional settings where M is large. Recalling the illustrative example in Figure 2, we were able to successfully identify the true partitions using a generalized AR(1) structure for a moderately sized problem ($M = 100$ and $N = 100$) in the first simulation.

5 Estimating brain co-activation regions

5.1 ABIDE data and problem setup

We use our proposed Bayesian clustering approach for dependence structures to identify regions of co-activation in the ABIDE dataset [11]. We consider rfMRI connectivity between $M = 1000$ ROIs defined by the hierarchical multi-resolution parcellation introduced in [42]. From the various versions of the Schaefer parcellation, we specifically adopt the 17-network parcellation provided by [25]. Our goal is to investigate between-network functional connectivity by identifying clusters of correlated ROIs that display co-activation patterns in school-age, male children diagnosed with both ASD and ADHD relative to those without co-occurring ADHD. To achieve this, we compare two distinct groups of individuals selected from the same participating sites within the dataset. The first group consists of 21 school-age, male children diagnosed with both ASD and ADHD, referred to as the ASD-coADHD group. The second group comprises 52 school-age, male children diagnosed with ASD but without ADHD, referred to as the ASD-nonADHD group.

In each group, we denote the number of subjects as n . The length of the rfMRI time series with a lag of 2 for the ℓ -th subject is represented by T_ℓ . By incorporating a lag of 2, we ensure that the time points are sufficiently spaced apart and independent. The total length of the concatenated rfMRI outcomes for all n individuals is defined as $N = \sum_{\ell=1}^n T_\ell$. Specifically, for the ASD-coADHD group, $N = 1755$, and for the ASD-nonADHD group, $N = 4594$. As the rfMRI outcome is an average across voxels within each ROI, the outcomes are approximately independently multivariate Gaussian due to the Central Limit Theorem. The covariates $\mathbf{X}_i \in \mathbb{R}^n$, $i = 1, \dots, N$, correspond to $\mathbf{e}_\ell \in \mathbb{R}^n$ for each $\ell \in \{1, \dots, n\}$. This representation gives a covariate corresponding to the indicator that the i -th outcome belongs to a time point for the ℓ -th individual. The rfMRI time series $\mathbf{Y}(\mathcal{S})$ are centered and scaled. We assume the covariance of $\mathbf{Y}(\mathcal{S})$ is block-diagonal with blocks following the compound symmetric (CS) model. This choice is motivated by our interest in exploring functional connectivity between ROIs, which does not necessarily depend on spatial

distance between the ROIs.

5.2 Results from estimating functional connectivity

For both the ASD-coADHD group and the ASD-nonADHD group separately, we perform MCMC runs for 14,000 iterations, with a burn-in of 4,000 iterations, for each of 50 different seeds. The MCMC tuning parameters and prior specifications are set to be consistent with those in Section 4. The results obtained from the 50 different seeds are combined to obtain the maximum a posteriori (MAP) estimate of \mathbf{Z} and an estimate of the posterior mode for $\boldsymbol{\rho}$ conditioned on the MAP estimate of \mathbf{Z} . To evaluate the convergence of the sampler, we investigated traceplots and autocorrelation functions of the covariance parameters.

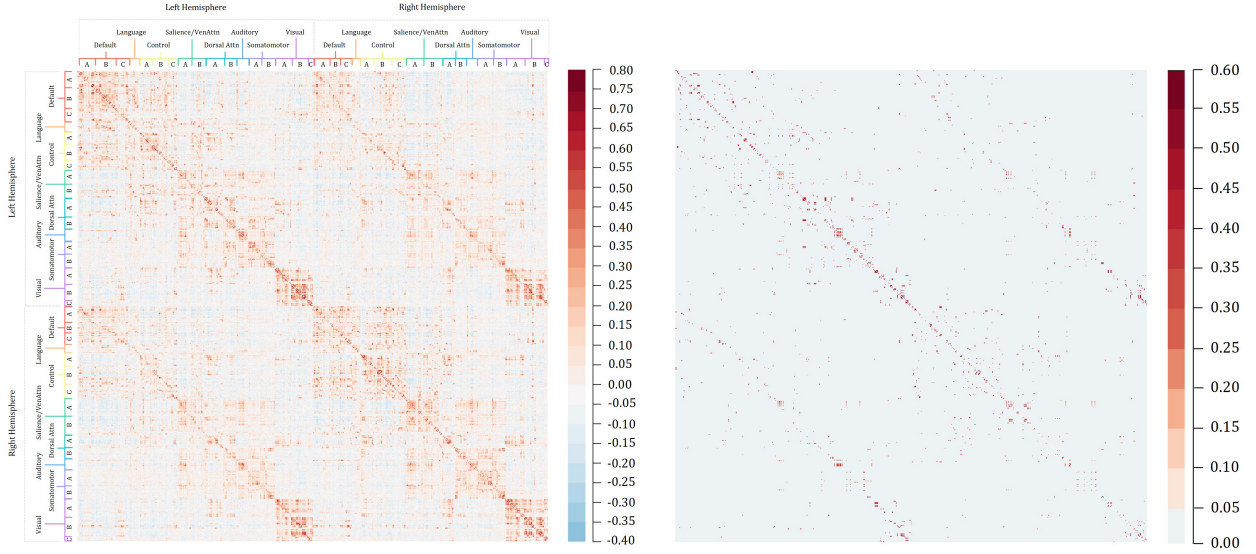


Figure 7: Sample correlation matrix (left) and the estimated correlation matrix (right) for the ASD-coADHD group. The initial 500 ROIs correspond to the 17 networks of the left hemisphere, while the latter 500 ROIs correspond to the 17 networks of the right hemisphere.

Figure 7 displays the sample correlation matrix and the estimated correlation matrix for the ASD-coADHD group. We can visually identify co-activation patterns highlighted in red along both the diagonals and the off-diagonals, forming a banded structure. By the ordering of ROIs in the 17-network parcellation, the first 500 ROIs correspond to the 17 networks of the left hemisphere, while the last 500 ROIs correspond to the 17 networks of the right hemisphere. Consequently, we can interpret the co-activation patterns along the diagonals as indicative of functional connectivity within each hemisphere, and the co-activation patterns along the off-diagonals as indicative of functional connectivity between the two hemispheres. Visual examination of the estimated correlation matrix shows that our proposed approach effectively captures the banded structure of the co-activation patterns observed in the sample correlation matrix. The plots for the ASD-nonADHD group are provided in Section 3 of the Supplementary Material.

5.3 Interpreting functional connectivity between networks

Our aim is to identify sets of positively correlated or co-activated ROIs that are specific to the ASD-coADHD group. To accomplish this, we compute a posterior similarity matrix where each entry represents the probability that pairs of ROIs belong to the same cluster. These probabilities are derived from empirically estimated posterior probabilities obtained through MCMC runs. See Section 3 of the Supplementary Material for the similarity matrices of the ASD-coADHD group and the ASD-nonADHD group. To achieve the highest possible accuracy in identifying correlated groups of ROIs, we focus on pairwise similarities where the similarity value is equal to or greater than 90%. Subsequently, we exclude similarity pairs that appear in both the ASD-coADHD and ASD-nonADHD groups, as these pairs indicate connections shared by both groups.

From the identified correlated groups of ROIs, we examine the functional connectivity between the 17 networks. The results of this analysis are summarized in Figure 8. In the figure, the number of ROIs connecting each network (9 out of 17) to the other 17 networks is presented. For the remaining 8 out of 17 networks, the results are detailed in Section 3 of the Supplementary Material.

Our findings are consistent with prior reports of multinet network atypicalities in ADHD [6] and ASD [15, 38] that involve both subnetwork and internetwork connectivity. Unlike prior work primarily focusing on pairwise relationships between networks, our approach has the advantage of jointly identifying sets of interconnected networks and subnetworks. Results in the ASD-coADHD group pointed towards greater involvement of default subnetworks connectivity and their connections with the language network, as well as connectivity between the control and attention networks. These two patterns of findings have been independently reported in ASD [15, 12] and ADHD [51, 48], suggesting that shared ASD- and ADHD-like patterns of atypical network connectivity exists in individuals with these frequent co-occurring conditions. Future studies with larger and well characterized samples of individuals with ASD, ADHD and their comorbidities are needed to confirm these findings.

6 Conclusions

In this paper, we have introduced a Bayesian clustering approach that effectively groups covariance submatrices associated with high-dimensional Gaussian outcomes. Our method incorporates the stick-breaking construction of the Dirichlet process prior, enabling the identification of independent subgroups of outcomes. We proposed a new Head-Tail Split-Merge sampler to achieve convergence of the MCMC. Through extensive simulations, we have validated the performance of our approach in settings involving large dimensions of M and J . Additionally, we have successfully applied our method to investigate co-activation patterns in ASD and ADHD, where we have discovered between-network functional connectivity patterns in the brain that align with findings in the existing literature.

In future research, it would be worthwhile to explore more comprehensive covariance structures to model functional connectivity in the brain for individuals with ASD. Possible directions include incorporating covariate effects into the covariance structure or considering ways to incorporate negative correlations in the covariance matrix. As observed in Figure 7, the sample correlation matrix exhibits not only co-activation patterns (positive correlation) but also reciprocal activation patterns (negative correlation). While the compound symmetry structure allows for negative correlations, its lower bound $-1/(M - 1)$ tends to zero as M increases, making it insufficient to capture reciprocal activation patterns. Further research in this area

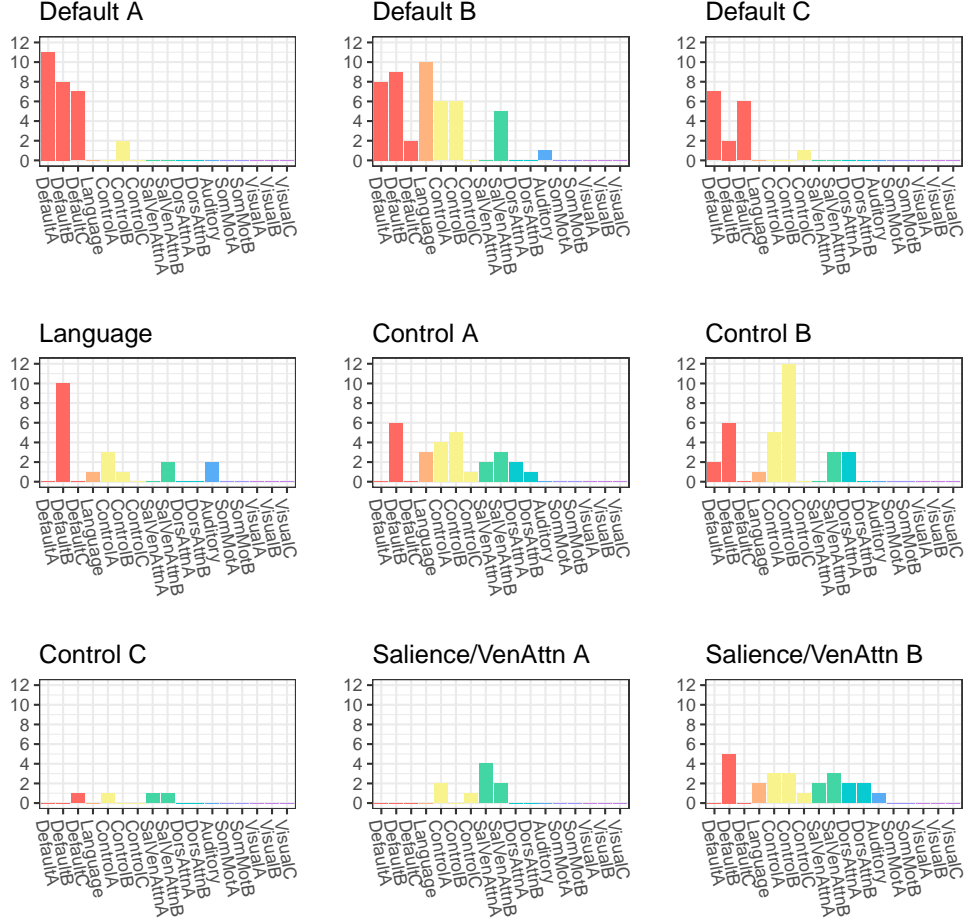


Figure 8: Summary of functional connectivity findings between the 17 networks. Plots of the number of ROIs connecting each network to the other 17 networks found in the ASD-coADHD group and not the ASD-nonADHD group.

could explore separate modeling of both types of patterns.

Acknowledgements

The authors are grateful to the participants of the ABIDE study, and the ABIDE study organizers and members who aggregated, preprocessed and shared the ABIDE data.

References

- [1] Sudipto Banerjee, Alan E. Gelfand, Andrew O. Finley, and Huiyan Sang. Gaussian predictive process models for large spatial data sets. *Journal of the Royal Statistical Society: Series B (Statistical*

- Methodology*, 70(5):825–848, 2008. doi: 10.1111/j.1467-9868.2008.00663.x. URL <https://doi.org/10.1111/j.1467-9868.2008.00663.x>.
- [2] Joanne C Beer, Howard J Aizenstein, Stewart J Anderson, and Robert T Krafty. Incorporating prior information with fused sparse group lasso: Application to prediction of clinical measures from neuroimages. *Biometrics*, 75(4):1299–1309, 12 2019. doi: 10.1111/biom.13075. URL <https://doi.org/10.1111/biom.13075>.
 - [3] Eric T Bell. Exponential numbers. *The American Mathematical Monthly*, 41(7):411–419, 1934.
 - [4] David M. Blei and Michael I. Jordan. Variational inference for dirichlet process mixtures. *Bayesian Analysis*, 1(1):121 – 143, 2006. doi: 10.1214/06-BA104. URL <https://doi.org/10.1214/06-BA104>.
 - [5] Alexandre Bouchard-Côté, Arnaud Doucet, and Andrew Roth. Particle gibbs split-merge sampling for bayesian inference in mixture models. *Journal of Machine Learning Research*, 18(28), 2017.
 - [6] F. Xavier Castellanos and Yuta Aoki. Intrinsic functional connectivity in attention-deficit/hyperactivity disorder: A science in development. *Biological Psychiatry Cognitive Neuroscience and Neuroimaging*, 1: 253–261, 2016. ISSN 2451-9022. doi: 10.1016/j.bpsc.2016.03.004.
 - [7] Jason Chang and John W Fisher III. Parallel sampling of dp mixture models using sub-cluster splits. In C.J. Burges, L. Bottou, M. Welling, Z. Ghahramani, and K.Q. Weinberger, editors, *Advances in Neural Information Processing Systems*, volume 26. Curran Associates, Inc., 2013. URL https://proceedings.neurips.cc/paper_files/paper/2013/file/bca82e41ee7b0833588399b1fcd177c7-Paper.pdf.
 - [8] Cameron Craddock, Yassine Benhajali, Carlton Chu, Francois Chouinard, Alan Evans, András Jakab, Budhachandra Singh Khundrakpam, John David Lewis, Qingyang Li, Michael Milham, et al. The neuro bureau preprocessing initiative: open sharing of preprocessed neuroimaging data and derivatives. *Frontiers in Neuroinformatics*, 7(27):5, 2013.
 - [9] David B Dahl. An improved merge-split sampler for conjugate dirichlet process mixture models. Technical report, University of Wisconsin - Madison, 2003.
 - [10] Sameer K. Deshpande, Veronika Ročková, and Edward I. George. Simultaneous variable and covariance selection with the multivariate spike-and-slab lasso. *Journal of Computational and Graphical Statistics*, 28(4):921–931, 2019. doi: 10.1080/10618600.2019.1593179. URL <https://doi.org/10.1080/10618600.2019.1593179>.
 - [11] Adriana Di Martino, Chao-Gan Yan, Qixiang Li, and et al. The autism brain imaging data exchange: towards a large-scale evaluation of the intrinsic brain architecture in autism. *Molecular Psychiatry*, 19(6):659–667, 2014. doi: 10.1038/mp.2013.78. URL <https://doi.org/10.1038/mp.2013.78>.
 - [12] Kristafor Farrant and Lucina Q Uddin. Atypical development of dorsal and ventral attention networks in autism. *Developmental Science*, 19:550–563, 2016. ISSN 1363-755X. doi: 10.1111/desc.12359.
 - [13] Thomas S. Ferguson. A bayesian analysis of some nonparametric problems. *The Annals of Statistics*, 1(2):209 – 230, 1973. doi: 10.1214/aos/1176342360. URL <https://doi.org/10.1214/aos/1176342360>.

- [14] Montserrat Fuentes. Approximate likelihood for large irregularly spaced spatial data. *Journal of the American Statistical Association*, 102(477):321–331, Mar 2007. doi: 10.1198/016214506000000852.
- [15] Yangfeifei Gao, Annika Linke, Ruth Joanne Jao Keehn, Sanjana Punyamurthula, Afroz Jahedi, Kathleen Gates, Inna Fishman, and Ralph-Axel Müller. The language network in autism: Atypical functional connectivity with default mode and visual regions. *Autism Research*, 12(9):1344–1355, 2019. ISSN 1939-3792. doi: 10.1002/aur.2171. URL <https://doi.org/10.1002/aur.2171>.
- [16] Sina Ghiassian, Russell Greiner, Ping Jin, and Matthew R G Brown. Using functional or structural magnetic resonance images and personal characteristic data to identify adhd and autism. *PLoS One*, 11(12):e0166934, 2016. ISSN 1932-6203. doi: 10.1371/journal.pone.0166934.
- [17] Peter J. Green and Sylvia Richardson. Modelling heterogeneity with and without the dirichlet process. *Scandinavian Journal of Statistics*, 28(2):355–375, 2001. ISSN 03036898, 14679469. URL <http://www.jstor.org/stable/4616664>.
- [18] Sungji Ha, In-Jung Sohn, Namwook Kim, Hyeon Jeong Sim, and Keun-Ah Cheon. Characteristics of brains in autism spectrum disorder: Structure, function and connectivity across the lifespan. *Experimental Neurobiology*, 24(4):273–284, 2015. doi: 10.5607/en.2015.24.4.273.
- [19] David I. Hastie, Silvia Liverani, and Sylvia Richardson. Sampling from dirichlet process mixture models with unknown concentration parameter: mixing issues in large data implementations. *Statistics and Computing*, 25(5):1023–1037, 2015. URL <https://doi.org/10.1007/s11222-014-9471-3>.
- [20] Jocelyn V Hull, Lisa B Dokovna, Zachary J Jacokes, Carinna M Torgerson, Andrei Irimia, and John Darrell Van Horn. Resting-state functional connectivity in autism spectrum disorders: A review. *Frontiers in psychiatry*, 7:205, 2016. doi: 10.3389/fpsy.2016.00205.
- [21] Hemant Ishwaran and Lancelot F James. Gibbs sampling methods for stick-breaking priors. *Journal of the American statistical Association*, 96(453):161–173, 2001.
- [22] Sonia Jain and Radford M. Neal. A split-merge markov chain monte carlo procedure for the dirichlet process mixture model. *Journal of Computational and Graphical Statistics*, 13(1):158–182, 2004. ISSN 10618600. URL <http://www.jstor.org/stable/1391150>.
- [23] Cari G. Kaufman, Mark J. Schervish, and Douglas W. Nychka. Covariance tapering for likelihood-based estimation in large spatial data sets. *Journal of the American Statistical Association*, 103(484):1545–1555, 2008. doi: 10.1198/016214508000000959.
- [24] Zakaria S. Khondker, Hongtu Zhu, Haitao Chu, Wei Lin, and Joseph G. Ibrahim. The bayesian covariance lasso. *Statistical Interface*, 6(2):243–259, Apr 2013. doi: 10.4310/sii.2013.v6.n2.a8.
- [25] Ru Kong, Qing Yang, Evan Gordon, Aihuiping Xue, Xiaoxuan Yan, Csaba Orban, Xi-Nian Zuo, Nathan Spreng, Tian Ge, Avram Holmes, Simon Eickhoff, and B T Thomas Yeo. Individual-specific areal-level parcellations improve functional connectivity prediction of behavior. *Cerebral Cortex*, 31(10):4477–4500, 05 2021. ISSN 1047-3211. doi: 10.1093/cercor/bhab101. URL <https://doi.org/10.1093/cercor/bhab101>.

- [26] Y. Li, B. Nan, and J. Zhu. Multivariate sparse group lasso for the multivariate multiple linear regression with an arbitrary group structure. *Biometrics*, 71(2):354–363, Jun 2015. doi: 10.1111/biom.12292. Epub 2015 Mar 2.
- [27] Yanxin Li and Stephen G Walker. A latent slice sampling algorithm. *Computational Statistics & Data Analysis*, 179:107652, 2023.
- [28] Shan Luo and Zehua Chen. Feature selection by canonical correlation search in high-dimensional multiresponse models with complex group structures. *Journal of the American Statistical Association*, 115(531):1227–1235, 2020. doi: 10.1080/01621459.2019.1609972.
- [29] Charles J Lynch, Lucina Q Uddin, Kaustubh Supekar, Amirah Khouzam, Jennifer Phillips, and Vinod Menon. Default mode network in childhood autism: posteromedial cortex heterogeneity and relationship with social deficits. *Biological psychiatry*, 74(3):212–219, 2013. doi: 10.1016/j.biopsych.2012.12.013.
- [30] Bertil Matérn. *Spatial Variation*. Lecture Notes in Statistics. Springer New York, NY, 2 edition, 1986. doi: 10.1007/978-1-4615-7892-5. Originally published by the Swedish National Institute for Forestry Research, 1960.
- [31] Kerrie L Mengersen and Richard L Tweedie. Rates of convergence of the hastings and metropolis algorithms. *The annals of Statistics*, 24(1):101–121, 1996.
- [32] Antonietta Mira and Luke Tierney. Efficiency and convergence properties of slice samplers. *Scandinavian Journal of Statistics*, 29(1):1–12, 2002. ISSN 03036898, 14679469. URL <http://www.jstor.org/stable/4616695>.
- [33] A. Mohammadi and E. C. Wit. Bayesian structure learning in sparse gaussian graphical models. *Bayesian Analysis*, 10(1):109 – 138, 2015. doi: 10.1214/14-BA889. URL <https://doi.org/10.1214/14-BA889>.
- [34] Sharon C Murray and Ronald W Helms. Linear models with generalized ar (1) covariance structure for irregularly-timed data. Technical report, North Carolina State University. Dept. of Statistics, 1990.
- [35] Radford M. Neal. Slice sampling. *The Annals of Statistics*, 31(3):705 – 767, 2003. doi: 10.1214/aos/1056562461. URL <https://doi.org/10.1214/aos/1056562461>.
- [36] Douglas Nychka, Soutir Bandyopadhyay, Dorit Hammerling, Finn Lindgren, and Stephan Sain. A multiresolution gaussian process model for the analysis of large spatial datasets. *Journal of Computational and Graphical Statistics*, 24(2):579–599, 2015. doi: 10.1080/10618600.2014.914946.
- [37] Omiros Papaspiliopoulos and Gareth O. Roberts. Retrospective markov chain monte carlo methods for dirichlet process hierarchical models. *Biometrika*, 95(1):169–186, 2008. ISSN 00063444, 14643510. URL <http://www.jstor.org/stable/20441450>.
- [38] Giorgia Picci, Stephen J Gotts, and K Suzanne Scherf. A theoretical rut: revisiting and critically evaluating the generalized under/over-connectivity hypothesis of autism. *Developmental science*, 19(4): 524–549, 2016.

- [39] Gareth O. Roberts and Jeffrey S. Rosenthal. Convergence of slice sampler markov chains. *Journal of the Royal Statistical Society. Series B (Statistical Methodology)*, 61(3):643–660, 1999. ISSN 13697412, 14679868. URL <http://www.jstor.org/stable/2680728>.
- [40] Alberto Roverato. Hyper inverse wishart distribution for non-decomposable graphs and its application to bayesian inference for gaussian graphical models. *Scandinavian Journal of Statistics*, 29(3):391–411, 2002. ISSN 03036898, 14679469. URL <http://www.jstor.org/stable/4616723>.
- [41] S. Samanta, K. Khare, and G. Michailidis. A generalized likelihood-based bayesian approach for scalable joint regression and covariance selection in high dimensions. *Statistical Computing*, 32(47), 2022. doi: 10.1007/s11222-022-10102-5. URL <https://doi.org/10.1007/s11222-022-10102-5>.
- [42] Alexander Schaefer, Ru Kong, Evan M. Gordon, Timothy O. Laumann, Xi-Nian Zuo, Avram J. Holmes, Simon B. Eickhoff, and B. T. Thomas Yeo. Local-global parcellation of the human cerebral cortex from intrinsic functional connectivity mri. *Cerebral Cortex*, 28(9):3095–3114, 2018. doi: 10.1093/cercor/bhx179.
- [43] Jayaram Sethuraman. A constructive definition of dirichlet priors. *Statistica Sinica*, 4(2):639–650, 1994. ISSN 10170405, 19968507. URL <http://www.jstor.org/stable/24305538>.
- [44] Michael L. Stein. Statistical properties of covariance tapers. *Journal of Computational and Graphical Statistics*, 22(4):866–885, 2013. doi: 10.1080/10618600.2012.719844.
- [45] Luke Tierney. Markov chains for exploring posterior distributions. *the Annals of Statistics*, pages 1701–1728, 1994.
- [46] Stephen G. Walker. Sampling unnormalized probabilities: An alternative to the metropolis-hastings algorithm. *SIAM Journal on Scientific Computing*, 36(2):A482–A494, 2014. doi: 10.1137/130922549. URL <https://doi.org/10.1137/130922549>.
- [47] Hao Wang. Bayesian Graphical Lasso Models and Efficient Posterior Computation. *Bayesian Analysis*, 7(4):867 – 886, 2012. doi: 10.1214/12-BA729. URL <https://doi.org/10.1214/12-BA729>.
- [48] Kai Wang, Ke Li, and Xiaoyu Niu. Altered functional connectivity in a triple-network model in autism with co-occurring attention deficit hyperactivity disorder. *Frontiers in Psychiatry*, 12:736755, 2021. ISSN 1664-0640. doi: 10.3389/fpsyt.2021.736755.
- [49] Wei Wang and Stuart J. Russell. A smart-dumb/dumb-smart algorithm for efficient split-merge mcmc. In *Conference on Uncertainty in Artificial Intelligence*, 2015.
- [50] Sinead Williamson, Avinava Dubey, and Eric Xing. Parallel markov chain monte carlo for nonparametric mixture models. In *International Conference on Machine Learning*, pages 98–106. PMLR, 2013.
- [51] Benjamin E Yerys, Evan M Gordon, Danielle N Abrams, Theodore D Satterthwaite, Rachel Weinblatt, Kathryn F Jankowski, John Strang, Lauren Kenworthy, William D Gaillard, and Chandan J Vaidya. Default mode network segregation and social deficits in autism spectrum disorder: Evidence from non-medicated children. *NeuroImage. Clinical*, 9:223–32, 2015. ISSN 2213-1582. doi: 10.1016/j.nicl.2015.07.018. URL <https://www.ncbi.nlm.nih.gov/pmc/articles/PMC4573091/>.

Supplementary Material

Bayesian estimation of clustered dependence structures in functional neuroconnectivity

Hyoshin Kim¹, Sujit K. Ghosh¹, Adriana Di Martino², and Emily C. Hector ^{*1}

¹Department of Statistics, North Carolina State University

²Autism Center, Child Mind Institute

1 Slice-within-Gibbs sampler for $V, \rho, \sigma^2, \alpha$, and B

This section provides a detailed explanation of the steps involved in running the Slice-within-Gibbs sampler to draw values from the conditional distributions of $V, \rho, \sigma^2, \alpha$, and B . The sampler iterates between the conditional distributions in the specified order. To commence, we introduce an expression for the likelihood which is used throughout the sampling algorithm.

1.1 Expression for the Likelihood

We present an alternative representation of the likelihood:

$$p\{\mathbf{Y}(\mathcal{S}) \mid \mathbf{B}, \mathbf{Z}, \rho, \sigma^2\} \propto \det\{\boldsymbol{\Sigma}(\mathcal{S}, \mathcal{S}; \boldsymbol{\theta})\}^{-N/2} \quad (1)$$

$$\cdot \exp\left[-\frac{1}{2} \sum_{i=1}^N \{\mathbf{y}_i(\mathcal{S}) - \mathbf{B}\mathbf{X}_i\}^\top \boldsymbol{\Sigma}(\mathcal{S}, \mathcal{S}; \boldsymbol{\theta})^{-1} \{\mathbf{y}_i(\mathcal{S}) - \mathbf{B}\mathbf{X}_i\}\right].$$

The determinant of $\boldsymbol{\Sigma}(\mathcal{S}, \mathcal{S}; \boldsymbol{\theta})$ in (1) can be expressed as

$$\det\{\boldsymbol{\Sigma}(\mathcal{S}, \mathcal{S}; \boldsymbol{\theta})\} \quad (2)$$

$$\propto \det\{\boldsymbol{\Sigma}_{\text{perm}}(\mathcal{S}, \mathcal{S}; \boldsymbol{\theta})\} = \prod_{j=1}^J \det\{\boldsymbol{\Sigma}_{\text{perm}}(\mathcal{S}_j, \mathcal{S}_j; \theta_j)\} = \prod_{j=1}^J \sigma_j^{2d_j} \det\{\boldsymbol{\Gamma}(\mathcal{S}_j, \mathcal{S}_j; \rho_j)\}.$$

Here, the terms involving the determinant of \mathbf{P}_π can be treated as constants since the determinant of a permutation matrix is either 1 or -1 . Denoting $\text{tr}(\cdot)$ the trace of a matrix, the terms within the exponential

^{*}Hector was supported by a grant from the National Science Foundation (DMS2152887) and a Faculty Research and Professional Development Award from North Carolina State University.

in equation (1) can be rewritten as

$$\begin{aligned}
& \sum_{i=1}^N \{\mathbf{y}_i(\mathcal{S}) - \mathbf{B}\mathbf{X}_i\}^\top \{\mathbf{P}_\pi^\top \boldsymbol{\Sigma}_{\text{perm}}(\mathcal{S}, \mathcal{S}; \boldsymbol{\theta}) \mathbf{P}_\pi\}^{-1} \{\mathbf{y}_i(\mathcal{S}) - \mathbf{B}\mathbf{X}_i\} \\
&= \sum_{i=1}^N \{\mathbf{y}_i(\mathcal{S}) - \mathbf{B}\mathbf{X}_i\}^\top \mathbf{P}_\pi^\top \boldsymbol{\Sigma}_{\text{perm}}^{-1}(\mathcal{S}, \mathcal{S}; \boldsymbol{\theta}) \mathbf{P}_\pi \{\mathbf{y}_i(\mathcal{S}) - \mathbf{B}\mathbf{X}_i\} \\
&= \text{tr}\{\mathbf{A} \boldsymbol{\Sigma}_{\text{perm}}^{-1}(\mathcal{S}, \mathcal{S}; \boldsymbol{\theta})\} \text{ where } \mathbf{A} = \mathbf{P}_\pi \left[\sum_{i=1}^N \{\mathbf{y}_i(\mathcal{S}) - \mathbf{B}\mathbf{X}_i\} \{\mathbf{y}_i(\mathcal{S}) - \mathbf{B}\mathbf{X}_i\}^\top \right] \mathbf{P}_\pi^\top \quad (3) \\
&= \sum_{j=1}^J \text{tr}\{\mathbf{A}_j \boldsymbol{\Sigma}_{\text{perm}}^{-1}(\mathcal{S}_j, \mathcal{S}_j; \theta_j)\} \text{ where } \mathbf{A}_j \in \mathbb{R}^{d_j \times d_j} \text{ is the } j^{\text{th}} \text{ diagonal block of } \mathbf{A} \\
&= \sum_{j=1}^J \sigma_j^{-2} \text{tr}\{\mathbf{A}_j \boldsymbol{\Gamma}^{-1}(\mathcal{S}_j, \mathcal{S}_j; \rho_j)\}.
\end{aligned}$$

The first equality follows from the fact that a permutation matrix is an orthogonal matrix. The computational challenges associated with calculating the expensive matrix inverse term $\boldsymbol{\Sigma}^{-1}$ can be avoided given the block-diagonal structure of $\boldsymbol{\Sigma}_{\text{perm}}^{-1}$. By combining terms in equations (2) and (3), the likelihood in equation (1) can be expressed as:

$$p\{\mathbf{Y}(\mathcal{S}) \mid \mathbf{B}, \mathbf{Z}, \boldsymbol{\rho}, \boldsymbol{\sigma}^2\} \propto \left[\prod_{j=1}^J \sigma_j^{2d_j} \det\{\boldsymbol{\Gamma}(\mathcal{S}_j, \mathcal{S}_j; \rho_j)\} \right]^{-N/2} \exp\left[-\frac{1}{2} \sum_{j=1}^J \sigma_j^{-2} \text{tr}\{\mathbf{A}_j \boldsymbol{\Gamma}^{-1}(\mathcal{S}_j, \mathcal{S}_j; \rho_j)\}\right].$$

1.2 Conditional for \mathbf{V}

By the conjugacy of the Beta distribution for \mathbf{V} and the categorical distribution for \mathbf{Z} , the conditional posterior distribution for \mathbf{V} is given by

$$\begin{aligned}
p(\mathbf{V} \mid \cdot) &\propto p(\mathbf{Z} \mid \mathbf{V}) p(\mathbf{V} \mid \alpha) \\
&\propto \prod_{j=1}^K \{w_j(\mathbf{V})^{m_j}\} \prod_{j=1}^{K-1} \{\alpha(1 - V_j)^{\alpha-1}\} \propto \prod_{j=1}^{K-1} \text{Beta}\left(1 + m_j, \alpha + \sum_{\ell=j+1}^K m_\ell\right).
\end{aligned}$$

Here, m_j represents the count of instances where $Z_m = j$ for $m = 1, \dots, M$, calculated as $m_j = \sum_{m=1}^M \mathbb{1}(Z_m = j)$. To obtain posterior samples of V_j for $j = 1, \dots, K-1$, we independently draw from the following distribution (recalling $V_K = 1$):

$$p(V_j \mid \cdot) \propto \text{Beta}\left(1 + m_j, \alpha + \sum_{\ell=j+1}^K m_\ell\right).$$

1.3 Conditional for ρ

The conditional posterior distribution for ρ can be written as follows:

$$\begin{aligned}
p(\rho | \cdot) &\propto p\{\mathbf{Y}(\mathcal{S}) | \mathbf{B}, \mathbf{Z}, \rho, \sigma^2\} p(\rho) \\
&\propto \prod_{j=1}^J \left[\det\{\mathbf{\Gamma}(\mathcal{S}_j, \mathcal{S}_j; \rho_j)\}^{-\frac{N}{2}} \exp\left[-\frac{1}{2\sigma_j^2} \text{tr}\{\mathbf{A}_j \mathbf{\Gamma}^{-1}(\mathcal{S}_j, \mathcal{S}_j; \rho_j)\}\right] \eta_j^{a_2-1} (1 - \eta_j)^{b_2-1} \right] \\
&\quad \prod_{j=J+1}^K \{\eta_j^{a_2-1} (1 - \eta_j)^{b_2-1}\}.
\end{aligned}$$

At each iteration, for $j = 1, \dots, J$, we independently sample ρ_j with

$$p(\rho_j | \cdot) \propto \det\{\mathbf{\Gamma}(\mathcal{S}_j, \mathcal{S}_j; \rho_j)\}^{-\frac{N}{2}} \exp\left[-\frac{1}{2\sigma_j^2} \text{tr}\{\mathbf{A}_j \mathbf{\Gamma}^{-1}(\mathcal{S}_j, \mathcal{S}_j; \rho_j)\}\right] \eta_j^{a_2-1} (1 - \eta_j)^{b_2-1}.$$

For $j = J + 1, \dots, K - 1$, we independently sample ρ_j from

$$p(\eta_j | \cdot) \propto \text{Beta}(a_2, b_2),$$

where η_j is the variable transformation of ρ_j . In the case where $d_j = 1$, we set $\rho_j = 0$ because the j -th sub-matrix has a dimension of one. This sampling procedure can be understood as follows: for $j = 1, \dots, J$, where the cluster membership of the j -th block is updated, we sample ρ_j by incorporating information from both the likelihood and the prior. However, for $j = J + 1, \dots, K$, where the cluster membership of the j -th block remains unchanged, we update ρ_j using only the prior information.

Algorithm 1 Li and Walker's slice sampler (Li and Walker, 2023) for ρ_j

Input: Current values of $\rho_0 := \rho_j$, step-size $s_0 := s_j$; variance tuning parameter λ ; support of $\rho_j \in (\rho_{\text{lb}}, \rho_{\text{ub}})$

Output: Proposed values of $\rho_j := \rho_1$ and $s_j := s_1$

1: Sample the slice variable $\omega \sim U(0, p(\rho_0 | \cdot))$, and sample

$$l_1 \sim U(\rho_0 - s_0/2, \rho_0 + s_0/2)$$

and s_1 from the density proportional to

$$\exp(-1/\lambda) \mathbb{1}(s_1 > 2|l_1 - \rho_0|)$$

2: If $\rho_{\text{lb}} < l_1 - s_1/2 < \rho_{\text{ub}}$ then set $a = l_1 - s_1/2$ else $a = \rho_{\text{lb}}$

If $\rho_{\text{lb}} < l_1 + s_1/2 < \rho_{\text{ub}}$ then set $b = l_1 + s_1/2$ else $b = \rho_{\text{ub}}$

3: Sample $\rho^* \sim U(a, b)$. If $p(\rho^* | \cdot) > \omega$, accept $\rho_1 = \rho^*$. Else,

$$\text{if } \rho^* < \rho_0 \text{ then } a = \max(a, \rho^*) \text{ else } b = \min(b, \rho^*)$$

4: Repeat Step 3 until $p(\rho^* | \cdot) > \omega$ and set $\rho_1 = \rho^*$

We propose to independently sample ρ_j , $j = 1, \dots, J$ in a Gibbs sampling framework using the slice sampler of [Li and Walker \(2023\)](#). A single iteration of Li and Walker’s slice sampler to generate a sample for ρ_j is described in Algorithm 1. Slice sampling is a popular method for generating samples from complex target densities when direct sampling is difficult. Compared to the Metropolis-Hastings algorithm, slice samplers do not require manually specifying the proposal distribution and are known to exhibit good convergence properties.

Li and Walker’s slice sampler is an extension of Neal’s slice sampler ([Neal, 2003](#)), with a modification made to the search component (Step 1 of Algorithm 1). The advantage of Li and Walker’s slice sampler lies in its flexibility and simplicity. Neal’s slice sampler uses a while-loop procedure with a fixed step size to search for the value of ρ_j to sample. In contrast, Li and Walker’s slice sampler adds flexibility by introducing a random step size s_j , eliminating the need for the while-loop component. The variance tuning parameter λ for s_j can be selected based on prior knowledge about the parameter’s support, with Li and Walker recommending a value of either 10 or 100.

1.4 Conditional for σ^2

By the conjugacy of the Gaussian likelihood and the Inverse-Gamma prior distribution for σ^2 , the conditional posterior distribution for σ^2 is given as

$$\begin{aligned} p(\sigma^2 | \cdot) &\propto p\{\mathbf{Y}(\mathcal{S}) | \mathbf{B}, \mathbf{Z}, \boldsymbol{\rho}, \sigma^2\} p(\sigma^2) \\ &\propto \prod_{j=1}^J \text{Inv-Gamma}\left\{a_1 + \frac{Nd_j}{2}, b_1 + \frac{1}{2} \text{tr}(\mathbf{A}_j \boldsymbol{\Gamma}^{-1}(\mathcal{S}_j, \mathcal{S}_j; \rho_j))\right\} \prod_{j=J+1}^K \text{Inv-Gamma}(a_1, b_1). \end{aligned}$$

In a similar manner to sampling the correlation parameters, we independently sample σ_j^2 at each iteration for $j = 1, \dots, J$ from

$$p(\sigma_j^2 | \cdot) \propto \text{Inv-Gamma}\left\{a_1 + \frac{Nd_j}{2}, b_1 + \frac{1}{2} \text{tr}(\mathbf{A}_j \boldsymbol{\Gamma}^{-1}(\mathcal{S}_j, \mathcal{S}_j; \rho_j))\right\}.$$

For $j = J + 1, \dots, K - 1$, we independently sample σ_j^2 from:

$$p(\sigma_j^2 | \cdot) \propto \text{Inv-Gamma}(a_1, b_1).$$

1.5 Conditional for α

By the conjugacy of the Beta prior distribution for \mathbf{V} and the Gamma prior distribution for α , we sample from the conditional posterior distribution for α , given by

$$p(\alpha | \cdot) \propto p(\mathbf{V} | \alpha) p(\alpha) \propto \text{Gamma}\left\{a_0 + K - 1, b_0 - \sum_{j=1}^{K-1} \log(1 - V_j)\right\}.$$

1.6 Conditional for $\text{vec}(\mathbf{B})$

The form of the conditional posterior distribution for $\text{vec}(\mathbf{B})$ can be derived as follows. First, we re-express the mean model as:

$$\mathbf{B}\mathbf{X}_i = \left\{ \text{diag}_M(X_{i1}) \quad \dots \quad \text{diag}_M(X_{ip}) \right\} \begin{pmatrix} \beta_1 \\ \vdots \\ \beta_p \end{pmatrix} = (\mathbf{X}_i^\top \otimes \mathbf{I}_M) \text{vec}(\mathbf{B}) = \tilde{\mathbf{X}}_i \text{vec}(\mathbf{B}).$$

Here, $\text{diag}_M(X_{iq})$ represents a diagonal matrix of dimension M with equal diagonal entries X_{iq} , $\tilde{\mathbf{X}}_i = (\mathbf{X}_i^\top \otimes \mathbf{I}_M) \in \mathbb{R}^{M \times Mp}$ and $\text{vec}(\mathbf{B}) \in \mathbb{R}^{Mp}$. To simplify notation, we denote $\boldsymbol{\Sigma} := \boldsymbol{\Sigma}(\mathcal{S}, \mathcal{S}; \boldsymbol{\theta})$ and $\boldsymbol{\Sigma}_{\text{perm}} := \boldsymbol{\Sigma}_{\text{perm}}(\mathcal{S}, \mathcal{S}; \boldsymbol{\theta})$. By the conjugacy of the Gaussian likelihood and the Gaussian prior distribution of $\text{vec}(\mathbf{B})$, the conditional posterior distribution for $\text{vec}(\mathbf{B})$ follows the multivariate Gaussian density

$$p\{\text{vec}(\mathbf{B}) | \cdot\} \propto p\{\mathbf{Y}(\mathcal{S}) | \mathbf{B}, \mathbf{Z}, \boldsymbol{\rho}, \boldsymbol{\sigma}^2\} p\{\text{vec}(\mathbf{B})\} \propto \mathcal{N}_{Mp}(\boldsymbol{\mu}, \boldsymbol{\Xi}),$$

where $\boldsymbol{\Xi}^{-1} := \boldsymbol{\Xi}^{-1}(\mathcal{S}, \mathcal{S}; \boldsymbol{\theta})$ and $\boldsymbol{\mu} := \boldsymbol{\mu}(\mathcal{S}; \boldsymbol{\theta})$ are defined as

$$\boldsymbol{\Xi}^{-1} = \sum_{i=1}^N \tilde{\mathbf{X}}_i^\top \boldsymbol{\Sigma}^{-1} \tilde{\mathbf{X}}_i + \tau^{-2} \mathbf{I}_{Mp}, \quad \boldsymbol{\mu} = \boldsymbol{\Xi} \sum_{i=1}^N \tilde{\mathbf{X}}_i^\top \boldsymbol{\Sigma}^{-1} \mathbf{y}_i(\mathcal{S}).$$

We further simplify the forms of $\boldsymbol{\Xi}^{-1}$, $\boldsymbol{\Xi}$ and $\boldsymbol{\mu}$ to avoid expensive matrix inverse calculations involving $\boldsymbol{\Sigma}^{-1}$. We can express $\boldsymbol{\Xi}^{-1}$ as a product of Kronecker products

$$\begin{aligned} \boldsymbol{\Xi}^{-1} &= (\mathbf{I}_p \otimes \boldsymbol{\Sigma}^{-1}) \sum_{i=1}^N \tilde{\mathbf{X}}_i^\top \tilde{\mathbf{X}}_i + \tau^{-2} \mathbf{I}_{Mp} \\ &= (\mathbf{I}_p \otimes \boldsymbol{\Sigma}^{-1}) \left(\sum_{i=1}^N \mathbf{X}_i \mathbf{X}_i^\top \otimes \mathbf{I}_M \right) + \tau^{-2} \mathbf{I}_{Mp} \\ &= \left(\sum_{i=1}^N \mathbf{X}_i \mathbf{X}_i^\top \otimes (\mathbf{P}_\pi^\top \boldsymbol{\Sigma}_{\text{perm}}^{-1} \mathbf{P}_\pi) \right) + \tau^{-2} \mathbf{I}_{Mp} \\ &= (\mathbf{I}_p \otimes \mathbf{P}_\pi^\top) \left(\sum_{i=1}^N \mathbf{X}_i \mathbf{X}_i^\top \otimes \boldsymbol{\Sigma}_{\text{perm}}^{-1} \right) (\mathbf{I}_p \otimes \mathbf{P}_\pi) + \tau^{-2} (\mathbf{I}_p \otimes \mathbf{P}_\pi^\top) (\mathbf{I}_p \otimes \mathbf{P}_\pi) \\ &= (\mathbf{I}_p \otimes \mathbf{P}_\pi^\top) \left(\sum_{i=1}^N \mathbf{X}_i \mathbf{X}_i^\top \otimes \boldsymbol{\Sigma}_{\text{perm}}^{-1} + \tau^{-2} \mathbf{I}_{Mp} \right) (\mathbf{I}_p \otimes \mathbf{P}_\pi), \end{aligned}$$

where the first equality follows from noting that $\tilde{\mathbf{X}}_i$ is a block matrix composed of row binding $\text{diag}_M(X_{iq})$, $q = 1, \dots, p$. The eigendecomposition of the $p \times p$ real symmetric matrix $\sum_{i=1}^N \mathbf{X}_i \mathbf{X}_i^\top$ and the $M \times M$ real symmetric matrix $\boldsymbol{\Sigma}_{\text{perm}}^{-1}$ yields $\sum_{i=1}^N \mathbf{X}_i \mathbf{X}_i^\top = \mathbf{Q}_1 \boldsymbol{\Lambda}_1 \mathbf{Q}_1^\top$ and $\boldsymbol{\Sigma}_{\text{perm}}^{-1} = \mathbf{Q}_2 \boldsymbol{\Lambda}_2 \mathbf{Q}_2^\top$, respectively. Here, $\boldsymbol{\Lambda}_1$ and $\boldsymbol{\Lambda}_2$ are diagonal matrices, and \mathbf{Q}_1 and \mathbf{Q}_2 are orthogonal matrices. Substituting these expressions into $\boldsymbol{\Xi}$

yields

$$\begin{aligned}
\Xi &= (\mathbf{I}_p \otimes \mathbf{P}_\pi^\top) \left(\sum_{i=1}^N \mathbf{X}_i \mathbf{X}_i^\top \otimes \Sigma_{\text{perm}}^{-1} + \tau^{-2} \mathbf{I}_{Mp} \right)^{-1} (\mathbf{I}_p \otimes \mathbf{P}_\pi) \\
&= (\mathbf{I}_p \otimes \mathbf{P}_\pi^\top) (\mathbf{Q}_1 \otimes \mathbf{Q}_2) (\Lambda_1 \otimes \Lambda_2 + \tau^{-2} \mathbf{I}_{Mp})^{-1} (\mathbf{Q}_1 \otimes \mathbf{Q}_2)^\top (\mathbf{I}_p \otimes \mathbf{P}_\pi) \\
&= (\mathbf{Q}_1 \otimes \mathbf{P}_\pi^\top \mathbf{Q}_2) (\Lambda_1 \otimes \Lambda_2 + \tau^{-2} \mathbf{I}_{Mp})^{-1} (\mathbf{Q}_1 \otimes \mathbf{P}_\pi^\top \mathbf{Q}_2)^\top \\
&= \mathbf{U} \mathbf{U}^\top
\end{aligned} \tag{4}$$

where $\mathbf{U} := (\mathbf{Q}_1 \otimes \mathbf{P}_\pi^\top \mathbf{Q}_2) (\Lambda_1 \otimes \Lambda_2 + \tau^{-2} \mathbf{I}_{Mp})^{-1/2}$. This reduces the computationally intensive inverse of a $Mp \times Mp$ matrix to a computation of the inverse square root of the diagonal matrix \mathbf{U} . Since $\Sigma_{\text{perm}}^{-1}$ is a block diagonal matrix, we can reduce computational time by separately performing the eigendecomposition of each main diagonal block to obtain \mathbf{Q}_2 and Λ_2 . The eigendecomposition for $\sum_{i=1}^N \mathbf{X}_i \mathbf{X}_i^\top$ is performed once at the beginning of the sampling algorithm. Similarly, we express $\boldsymbol{\mu}$ as follows:

$$\begin{aligned}
\boldsymbol{\mu} &= \Xi \sum_{i=1}^N (\mathbf{I}_p \otimes \Sigma^{-1}) (\mathbf{X}_i \otimes \mathbf{I}_M) \mathbf{y}_i(\mathcal{S}) \\
&= \Xi \sum_{i=1}^N (\mathbf{X}_i \otimes \Sigma^{-1}) \mathbf{y}_i(\mathcal{S}) \\
&= \Xi \text{vec} \left\{ \mathbf{P}_\pi^\top \Sigma_{\text{perm}}^{-1} \mathbf{P}_\pi \sum_{i=1}^N \mathbf{y}_i(\mathcal{S}) \mathbf{X}_i^\top \right\}.
\end{aligned} \tag{5}$$

Here, the last equality follows from the vectorization of the Kronecker product. By combining the terms in equations (4) and (5), we sample $\text{vec}(\mathbf{B})$ from the following distribution:

$$\text{vec}(\mathbf{B}) = \boldsymbol{\mu} + \mathbf{U} \boldsymbol{\nu}, \quad \boldsymbol{\nu} \sim \mathcal{N}_{Mp}(\mathbf{0}, \mathbf{I}_{Mp}).$$

2 Additional simulation outputs

2.1 First simulation

This section presents the results from the first simulation during the burn-in period. Figure 1 displays the average posterior distribution of \mathbf{Z} across 50 simulations for the three settings. As the complexity of the covariance structure increases, the average number of partitions visited also increases, while the posterior probability of the MAP decreases. This suggests that a greater number of iterations is needed to identify the true partition as the complexity increases. In addition, the 95% percentile intervals of the posterior probability of the MAP derived from the 50 simulations become wider with increasing complexity, indicating that some simulations fail to accurately identify the correct partition during the burn-in period.

Table 1 presents the average coverage rates for a 95% credible interval across 50 simulations for $\boldsymbol{\rho}, \sigma^2$, and \mathbf{B} during the burn-in period. The coverage rates are computed from the subset of iterations where \mathbf{Z} is equal to its MAP estimate. The results demonstrate that the desired 95% level is achieved for all three settings, with slightly conservative inference and greater variability compared to the sampling period.

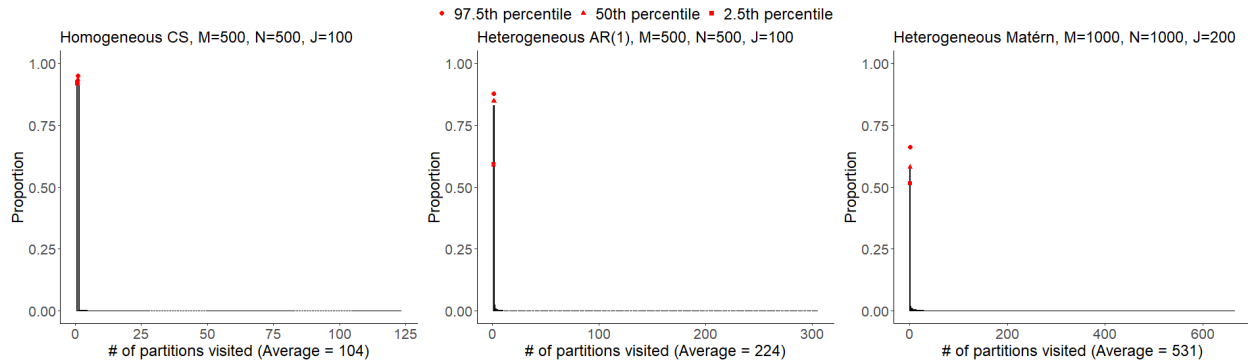


Figure 1: First simulation – Plot of posterior distribution of \mathbf{Z} averaged across 50 simulations during the burn-in period, assuming a uniform true partition. The red points are the 95% percentile intervals of the probability of MAPs across the 50 simulations.

Table 1: First simulation – Summary of coverage rates for a 95% credible interval, averaged across 50 simulations for $\rho, \sigma^2, \mathbf{B}$ during the burn-in period, assuming a uniform true partition. Standard deviations are in parentheses. The coverage rates are computed from the subset of iterations where \mathbf{Z} is equal to its MAP estimate.

	M	N	J	coverage rate (sd)		
				ρ	σ^2	\mathbf{B}
homogeneous CS	500	500	100	1.00 (0.00)	1.00 (0.00)	0.95 (0.01)
heterogeneous AR(1)	500	500	100	0.96 (0.07)	0.97 (0.05)	0.95 (0.01)
heterogeneous Matérn	1000	1000	200	0.96 (0.14)	0.97 (0.08)	0.95 (0.01)

2.2 Second simulation

Here we present results from the second simulation during the burn-in period.

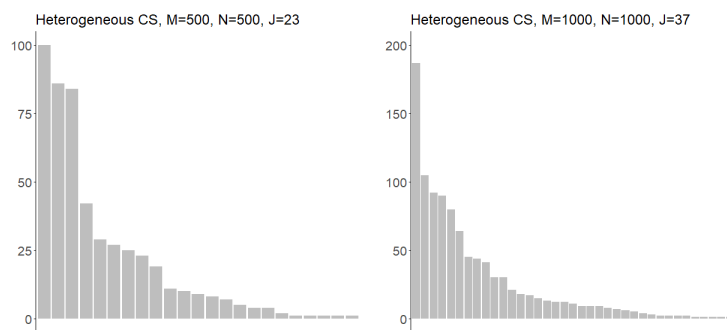


Figure 2: Second simulation – Plot of the true partition generated from a $DP(6, P_0)$. The partition labels are sorted by block size from largest to smallest.

Figure 3 shows that the average probability assigned to the MAP estimate is approximately 0.5 for both settings during the burn-in period, due to the proposed HTSM algorithm's tail moves during the second phase of the MCMC. As the true partition has a moderate amount of size one clusters, the sampler mostly identifies the true partition during the second phase. Note that in the first simulation, the true partition was mostly identified during the first phase, leading to higher posterior probability of the MAPs than the second

simulation.

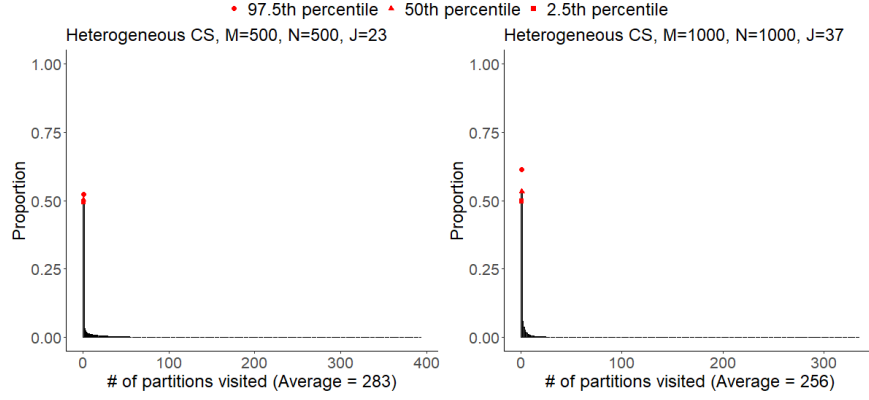


Figure 3: Second simulation – Plot of posterior distribution of \mathbf{Z} averaged across 50 simulations during the burn-in period, assuming a $DP(6, P_0)$ true partition. The red points are the 95% percentile intervals of the probability of MAPs across the 50 simulations.

Table 2 shows that the desired 95% level is achieved for the average coverage rates of credible intervals across 50 simulations for ρ, σ^2 , and \mathbf{B} during the burn-in period, with greater variability compared to the sampling phase.

Table 2: Second simulation – Summary of coverage rates for a 95% credible interval, averaged across 50 simulations for $\rho, \sigma^2, \mathbf{B}$ during the burn-in period, assuming a $DP(6, P_0)$ true partition. Standard deviations are in parentheses. The coverage rates are computed from the subset of iterations where \mathbf{Z} is equal to its MAP estimate.

	M	N	J	coverage rate (sd)		
				ρ	σ^2	\mathbf{B}
heterogeneous CS	500	500	23	0.99 (0.02)	0.97 (0.03)	0.95 (0.02)
heterogeneous CS	1000	1000	37	0.99 (0.02)	0.97 (0.03)	0.95 (0.01)

3 Additional data analysis outputs

This section presents additional data analysis outputs. Figure 4 shows that the autocorrelation of the rfMRI time series outcomes diminishes to zero, indicating that the outcomes can be treated as independent.

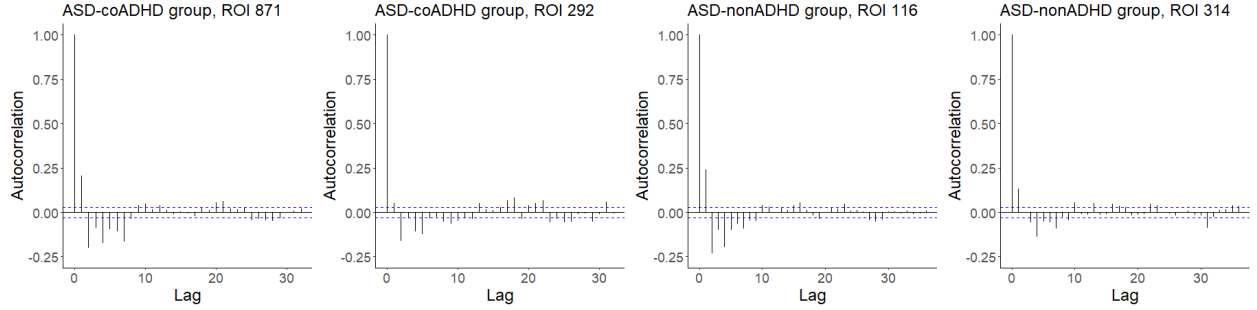


Figure 4: Autocorrelation functions of the rfMRI time series with a lag of 2 for the ASD-coADHD group and the ASD-nonADHD group, on randomly selected ROIs.

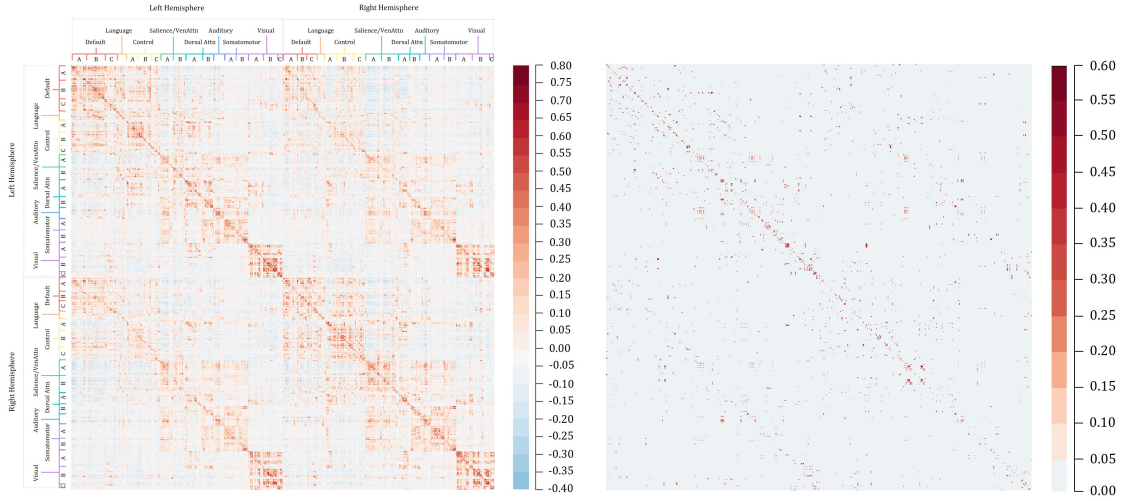


Figure 5: Connectivity matrix (left) and the estimated correlation matrix (right) for the ASD-nonADHD group. The initial 500 ROIs correspond to the 17 networks of the left hemisphere, while the latter 500 ROIs correspond to the 17 networks of the right hemisphere.

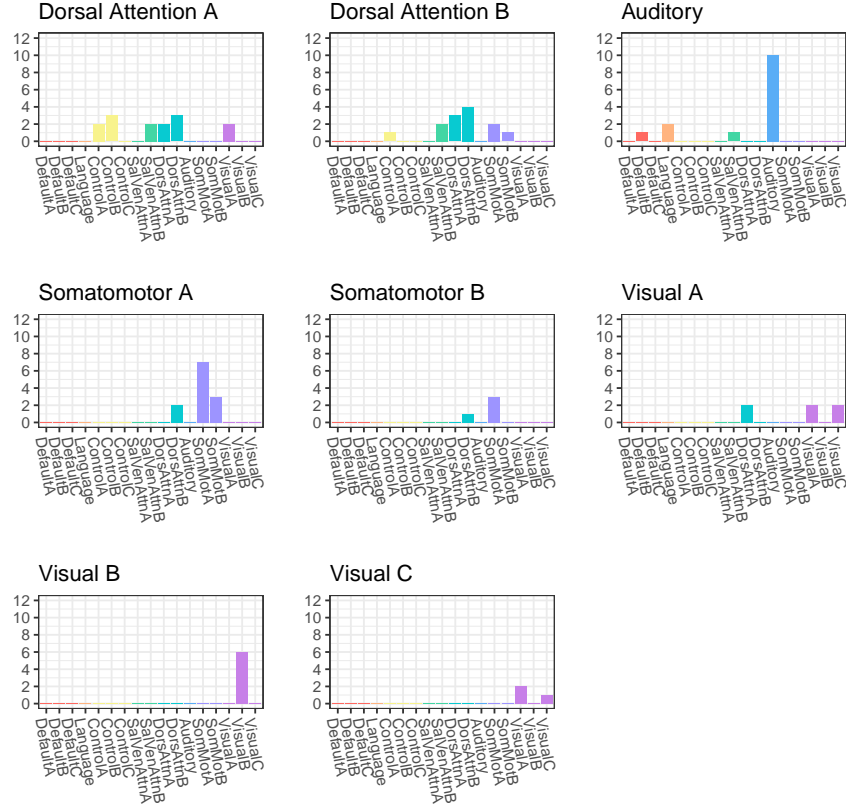


Figure 6: Summary of functional connectivity findings between the 17 networks. Plots of the number of ROIs connecting each network to the other 17 networks found in the ASD-coADHD group and not the ASD-nonADHD group.

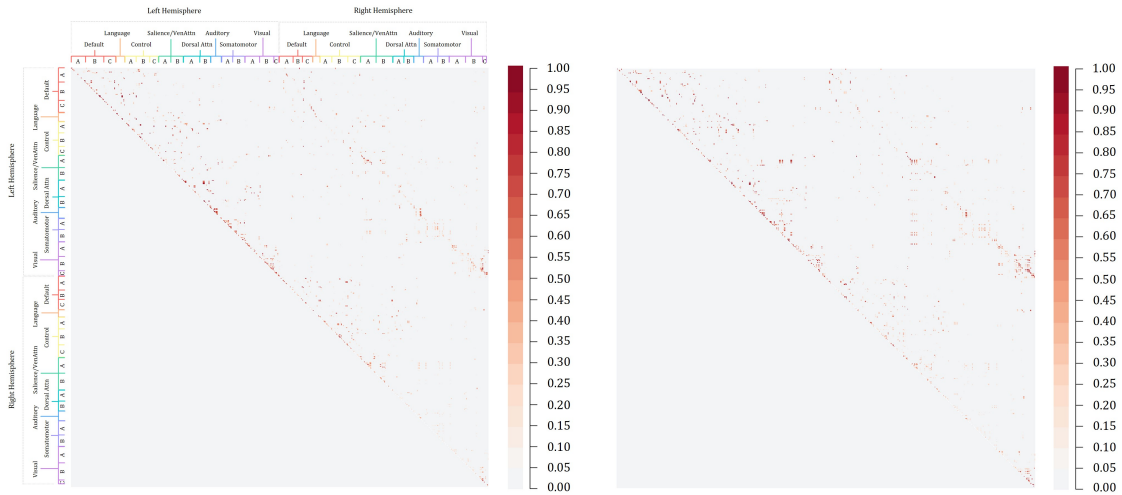


Figure 7: Posterior similarity matrix indicating the probability that pairs of ROIs belong to the same cluster for the ASD-coADHD group (left) and for the ASD-nonADHD group (right).

References

- Yanxin Li and Stephen G Walker. A latent slice sampling algorithm. *Computational Statistics & Data Analysis*, 179:107652, 2023.
- Radford M. Neal. Slice sampling. *The Annals of Statistics*, 31(3):705 – 767, 2003. doi: 10.1214/aos/1056562461.
URL <https://doi.org/10.1214/aos/1056562461>.